

unWISE tomography of Planck CMB lensing

Alex Krolewski^{b,c} Simone Ferraro^b Edward F. Schlafly^b Martin White^{a,b,c}

^aDepartment of Physics, University of California, Berkeley, CA 94720

^bPhysics Division, Lawrence Berkeley National Laboratory, Berkeley, CA

^cDepartment of Astronomy, University of California, Berkeley, CA 94720

E-mail: krolewski@berkeley.edu, sferraro@lbl.gov, eschlafly@lbl.gov,
mwhite@berkeley.edu

Abstract. CMB lensing tomography, or the cross-correlation between CMB lensing maps and large-scale structure tracers over a well-defined redshift range, has the potential to map the amplitude and growth of structure over cosmic time, provide some of the most stringent tests of gravity, and break important degeneracies between cosmological parameters. In this work, we use the unWISE galaxy catalog to provide three samples at median redshifts $z \sim 0.6, 1.1$ and 1.5 , fully spanning the Dark Energy dominated era, together with the most recent Planck CMB lensing maps. We obtain a combined cross-correlation significance $S/N = 79.3$ over the range of scales $100 < \ell < 1000$. We measure the redshift distribution of unWISE sources by a combination of cross-matching with the COSMOS photometric catalog and cross-correlation with BOSS galaxies and quasars and eBOSS quasars. We also show that magnification bias must be included in our analysis and perform a number of null tests. In a companion paper, we explore the derived cosmological parameters by modeling the non-linearities and propagating the redshift distribution uncertainties.

Keywords: cosmological parameters from LSS – power spectrum – CMB – galaxy clustering

ArXiv ePrint: [19MM.NNNNN](https://arxiv.org/abs/19MM.NNNNN)

Contents

1	Introduction	1
2	The data	2
2.1	Planck CMB lensing maps	2
2.2	unWISE	4
2.3	Galaxy selection	4
2.4	Masks	5
3	Model	6
3.1	Angular Clustering	6
3.2	HaloFit model	7
4	Angular clustering	8
4.1	Angular power spectra estimation	8
4.2	Covariance matrix	10
5	Galaxy redshift distribution	11
5.1	Cross-match redshifts	11
5.2	Cross-correlation redshifts	13
5.3	Systematic errors in the cross-correlation dN/dz	21
6	Galaxy-lensing auto and cross-spectra	22
7	Systematics in the cross-correlation and null tests	23
7.1	Stellar Contamination	23
7.2	Foreground contamination to CMB lensing cross-correlations	25
7.3	Galactic mask dependence of the sample properties	26
7.4	Systematic uncertainties in the redshift distribution	27
8	Conclusions and lessons learned	30
A	Optical properties of unWISE samples and prospects for spectroscopic followup	33
B	Simple HOD model for unWISE samples	35
C	Response of the number density to magnification bias	41
D	Galaxy-galaxy cross spectra	42

1 Introduction

As they travel from the surface of last scattering to the Earth, Cosmic Microwave Background (CMB) photons are deflected by the gravitational potentials associated with large-scale structure (LSS), providing a probe of late-time physics directly in the CMB sky (see Refs. [1, 2] for

reviews). The lensing effect is dominated by structures on Mpc scales over a very broad range of redshifts from $z < 1$ to $z \sim 10$. By cross-correlating the lensing map with another tracer of large-scale structure which spans a narrower range in redshift, we can simultaneously increase the signal-to-noise ratio and isolate particular redshifts of interest. Doing this on multiple lens redshift planes (“CMB lensing tomography”) breaks important degeneracies between the expansion history and the growth of perturbations, as well as providing greater control over systematics [3, 4]. The first detections of CMB lensing were obtained in cross-correlation between galaxy samples and WMAP data [5, 6], and some of the early work employing cross-correlations with ACT, SPT and Planck are presented in refs. [7–9] respectively. Since then, there have been a large number of cross-correlation analysis with a wide variety of samples (see for example refs. [10–16]).

In this work, we use galaxies from the unWISE catalog [17], containing angular positions and magnitudes of over two billion objects observed by the Wide-field Infrared Survey Explorer (WISE, [18]) mission. The unWISE catalog builds upon earlier WISE-based catalogs by including additional data from the post-hibernation NEOWISE mission, and is the largest full-sky galaxy catalog currently available [17], containing over half a billion galaxies across the full sky. We further divide the catalog based on magnitude and color and reject stars based on Gaia data [19], creating three samples, referred here as “blue”, “green” and “red,” at median redshifts $\sim 0.6, 1.1$ and 1.5 , respectively, allowing a tomographic analysis of the amplitude of fluctuations in the Dark Energy dominated era. Previous cross-correlations between WISE-derived catalogs and CMB lensing were presented in refs. [9, 16, 20–24].

In this paper, we present the auto correlation of the galaxy samples and their cross-correlation with the Planck CMB lensing maps [25]. We also measure the redshift distribution of the unWISE galaxies, which is crucial for the cosmological interpretation of the signal. While obtaining photometric redshifts from the two WISE colors alone is not feasible, cross-matching sources with the COSMOS photometric catalog as well as cross correlation with a number of spectroscopic surveys allows us to determine the ensemble redshift distribution of our samples, together with an estimate of its uncertainty.

The outline of the paper is as follows: In Section 2 we summarize the data used and in Section 3 we describe our modelling. In Section 4 we discuss the auto and cross correlation measurements and in Section 5, we measure the redshift distribution of the unWISE sample and characterize its uncertainties. The results are presented in Section 6. Possible systematics and null tests are explored in Section 7, and in Section 8 we summarize our results. This paper is focused on the measurement of the cross-correlation. In a companion paper [26], we will extract cosmological information by modeling the non-linearities in the signal and marginalizing over uncertainties in the stellar contamination fraction and the galaxy redshift distribution.

Where necessary we assume a fiducial Λ CDM cosmology with the Planck 2018 maximum likelihood parameters (the final column in Table 2 in ref. [27]). We quote magnitudes in the Vega system, noting that we can easily convert these to AB magnitudes with $AB = Vega + 2.699, 3.339$ in W1, W2, respectively.

2 The data

2.1 Planck CMB lensing maps

Gravitational lensing of the CMB remaps the temperature and polarization fields, altering their statistics in a well-defined way [1]. By searching for these statistical patterns it is possi-

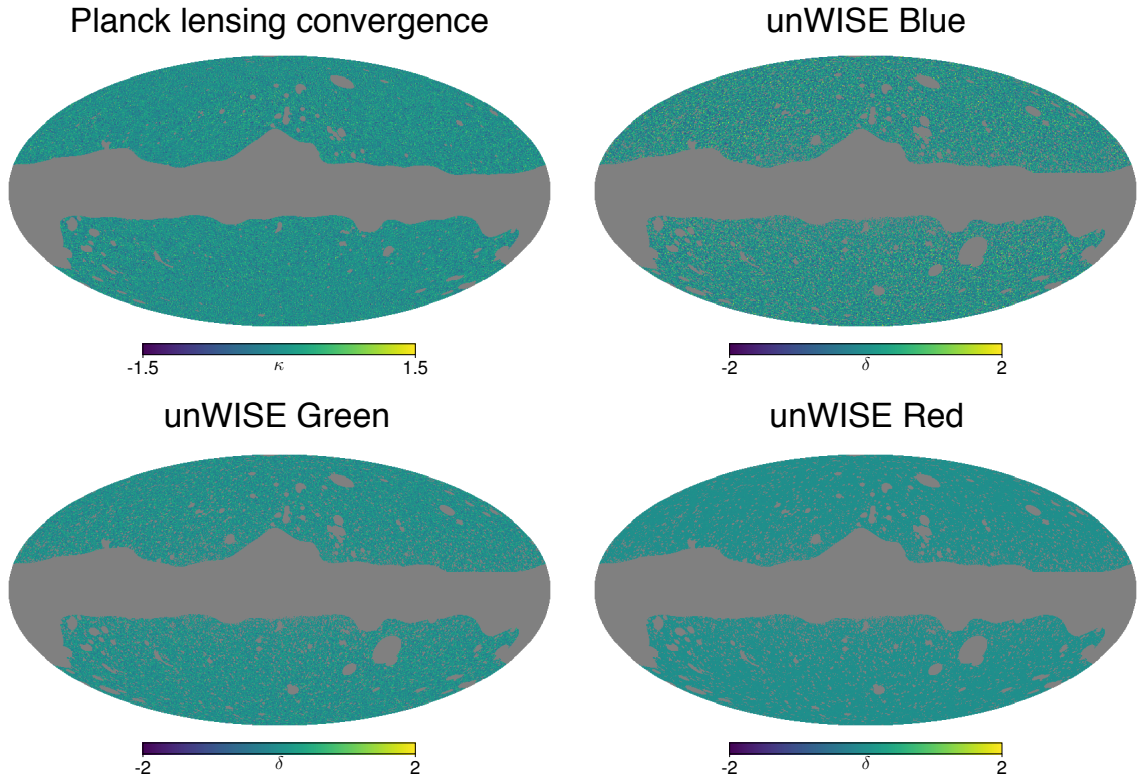


Figure 1. Plot of the maps used in the analysis (κ for Planck lensing convergence and density contrast δ for the galaxy samples). The maps have been filtered to only contain the range of scales used in this analysis, i.e. $\ell_{\min} = 100$ and $\ell_{\max} = 1000$, and this explains the lack of large-scale power.

ble to reconstruct the lensing convergence, κ , from quadratic combinations of the foreground-cleaned maps [28]. We use the latest CMB lensing maps from the Planck 2018 release [25] and their associated masks, downloaded from the Planck Legacy Archive.¹ These maps are provided as spherical harmonic coefficients of the convergence, $\kappa_{\ell m}$, in HEALPix format [29] and with $\ell_{\max} = 4096$. In particular, for our fiducial analysis we use the minimum-variance (MV) estimate obtained from both temperature and polarization, based on the SMICA foreground-reduced CMB map. Since the MV reconstruction is dominated by temperature, residual galactic and extragalactic foregrounds may contaminate the signal. Extensive testing has been performed by the Planck team, indicating no significant problems at the current statistical level. Nonetheless, thermal Sunyaev-Zel’dovich (tSZ) contamination has been shown to be one of the largest potential contaminants to cross correlations with tracers of large-scale structure in other analyses [30–33]. For this reason, as a test, we shall repeat the analysis with a lensing reconstruction on SMICA foreground-reduced maps where tSZ has been explicitly deprojected [25], and we will refer to this analysis as “tSZ-free.” Possible foreground contamination is discussed more in detail in Section 7.2.

¹PLA: <https://pla.esac.esa.int/>

Label	$W1 - W2 > x$	$W1 - W2 < x$	$W2 < x$	\bar{z}	δz	\bar{n}	s
Blue		$(17 - W2)/4 + 0.3$	16.7	0.6	0.3	3409	0.455
Green	$(17 - W2)/4 + 0.3$	$(17 - W2)/4 + 0.8$	16.7	1.1	0.4	1846	0.648
Red	$(17 - W2)/4 + 0.8$		16.2	1.5	0.4	144	0.842

Table 1. Color and magnitude cuts for selecting galaxies of different redshifts, together with the mean redshift, \bar{z} , and the width of the redshift distribution, δz (as measured by matching to objects with photometric redshifts on the COSMOS field [41]), number density per deg^2 within the unWISE mask, \bar{n} , and response of the number density to magnification, $s \equiv d \log_{10} N/dm$. Galaxies are additionally required to have $W2 > 15.5$, to be undetected or not pointlike in Gaia (see §2.3), and to not be flagged as diffraction spikes, latents or ghosts. s is measured using galaxies at ecliptic latitude $|\lambda| > 60^\circ$, where WISE reaches fainter limiting magnitudes due to increased depth of coverage (see Appendix C).

2.2 unWISE

The WISE mission mapped the entire sky at 3.4, 4.6, 12, and 22 μm (W1, W2, W3, and W4) with angular resolutions of 6.1", 6.4", 6.5" and 12", respectively [18]. The AllWISE data release encompassed the full WISE cryogenic mission as well as the initial NEOWISE post-cryogenic mission, from 2010 January to 2011 February, after which the instrument was placed into hibernation [34, 35]. The W1 and W2 bands do not require cryogen to operate efficiently, motivating reactivation of WISE in December 2013 [36]. Observations from the continuing NEOWISE mission have been incorporated into increasingly deep “unWISE” coadded images of the sky [37–39], which now feature more than $4\times$ longer exposure times than were available for the AllWISE data release. In the future, at least another two years of NEOWISE data will be available (NEO5 and NEO6), which would further increase the depth by ~ 0.2 magnitudes.

The deeper imaging coupled with the $\sim 6.5''$ angular resolution leads to crowded images with many overlapping sources, requiring a new approach to the analysis of the WISE coadded images. The `crowdsourc` crowded field photometry pipeline [40], originally designed for surveys of the Galactic plane, was employed to generate a new catalog based on the deep unWISE coadded images [17]. The resulting catalog provides a sample of > 500 million galaxies with $0 < z < 2$ and improves the uniformity of the depth and photometric calibration of the WISE survey.

2.3 Galaxy selection

Galaxies are selected on the basis of their WISE W1 and W2 magnitudes. Inspection of the average colors of galaxies detected in WISE as a function of redshift shows a clear trend in which fainter and redder galaxies tend to be at higher redshift. Accordingly we made three selections of galaxies in $W1 - W2$ color, with a sliding cut on color with magnitude reflecting that fainter galaxies tend to be at higher redshifts. Table 1 gives the adopted color selection for the three samples considered in this work, which we term the blue, green, and red samples [17]. Table 1 also summarizes important properties of each sample including the redshift distribution, the number density, and the response of number density to galaxy magnification $s \equiv d \log_{10} N/dm$. We measure s using galaxies with ecliptic latitude $|\lambda| > 60^\circ$, where the WISE depth of coverage is greater and thus the measurement of s is less affected by incompleteness. We describe the measurement of s in Appendix C.

We require that the blue and green samples have $15.5 < W2 < 16.7$, and the red sample has $15.5 < W2 < 16.2$. If we allow the red sample to include sources with $16.2 < W2 < 16.7$, we find that the red-blue cross-correlation is inconsistent at the $2\text{-}3\sigma$ level with the expected

cross-correlation given the bias measured from the CMB-cross spectra (Appendix D). The fainter red samples also exhibit a decrease in number density closer to the Galactic plane, and may have more angular variation in dN/dz . As a result, we suspect that the fainter red sample is more affected by stellar contamination or systematics-driven fluctuations, and exclude it from our fiducial definition of the red sample.

Each of the samples is required to be either undetected or not pointlike in Gaia. Here a source is taken as “pointlike” if

$$\text{pointlike}(G, A) = \begin{cases} \log_{10} A < 0.5 & \text{if } G < 19.25 \\ \log_{10} A < 0.5 + \frac{5}{16}(G - 19.25) & \text{otherwise,} \end{cases} \quad (2.1)$$

where G is the Gaia G band magnitude and A is `astrometric_excess_noise` from Gaia DR2 [42]. A source is considered “undetected” in Gaia if there is no Gaia DR2 source within $2.75''$ of the location of the WISE source. High `astrometric_excess_noise` indicates that the Gaia astrometry of a source was more uncertain than typical for resolved sources; this cut essentially takes advantage of the $0.1''$ angular resolution of Gaia to morphologically separate point sources from galaxies. We additionally remove sources classified as diffraction spikes, first or second latents, or ghosts in either W1 or W2, corresponding to “unWISE flags” 1, 2, 3, 4 or 7.²

2.4 Masks

For the lensing map, we use the official 2018 Planck lensing mask, provided together with the other data products [25]. This is created using a combination of the SMICA 70% Galactic mask, retaining the cleanest 70% of the sky, together with the 143 and 217 GHz point source masks and the tSZ-detected clusters with $S/N > 5$ [25]. We additionally masked a small region of the sky with $|b| < 10^\circ$ that was unmasked in the Planck map. Overall, this leaves an unmasked sky fraction $f_{\text{sky}} = 0.670$ for the lensing map. As a test of Galactic contamination we also use the 60 and 40% temperature masks from the Planck 2018 data release³, masking an increasing fraction of the Galactic plane. The impact on the results is discussed in Section 7.3.

For WISE, we found it convenient to use the Planck lensing mask as an effective galactic mask, to avoid excessive stellar contamination close to the galactic plane. We additionally mask stars, galaxies, planetary nebulae, and `NSIDE` = 2048 HEALPix pixels with substantial area lost due to sub-pixel unWISE masks (e.g. for diffraction spikes from bright stars).

We mask the 6678 brightest stars in the infrared sky (6156 at $|b| > 20^\circ$) with $W1 < 2.5$ or $W2 < 2$ or $K < 2$ (where the WISE magnitude is the brighter of the AllWISE or unWISE magnitudes). We use the bright star list provided by the CatWISE team (Eisenhardt et al., in prep)⁴ for these objects.⁵ We find that a disk of radius 0.5° is adequate to prevent contamination due to spurious detections around the majority of these bright sources. For the very brightest stars, diffraction spikes extend beyond the $\sim 1^\circ$ extent of the diffraction spike mask; we therefore use a 1.5° radius around 32 stars with $-3 < W2 < -2$ and a 3° radius around 11 stars with $W2 < -3$. Finally, we mask 0.2° around 6212 stars with $2 < W2 < 2.5$,

²See Table 5 here: http://catalog.unwise.me/files/unwise_bitmask_writeup-03Dec2018.pdf

³Always multiplied by the original lensing mask.

⁴catwise.github.io

⁵We additionally add the carbon star IRC+20326, which had problematic photometry in both AllWISE and unWISE.

$W1 > 2.5$, and $K > 2$, where we find that in rare cases, the unWISE PSF model does not extend far enough into the wings of the star, leading to spurious sources at the edge of the modeled region.

We also mask bright galaxies using the LSLGA catalog⁶, selecting 715 galaxies from Hyperleda [43] with magnitudes < 13 (almost always in the B filter, though in rare cases the K or I filter), diameter $D_{25} > 3$ arcmin, and surface brightness within D_{25} of < 26 mag/arcsec². Using the position angle and ellipticity in the catalog we mask ellipses around each galaxy out to $1.5R_{25}$, and we visually confirm that this radius removes the impact of galaxies on our samples.

We also find that planetary nebulae can contaminate our samples, particularly the red sample. We mask 1143 planetary nebulae [44], masking out to twice the optical radius of each planetary nebula.

In all three cases (stars, galaxies, and planetary nebulae) we create a binary mask on an $\text{NSIDE} = 2048$ HEALPix map, masking all pixels within the specified distance of the source. For the planetary nebulae, we additionally use the “inclusive=True” option in the HEALPix `QUERY_DISC` command since the pixels in our map are often larger than the mask radius.

Finally, we correct for area lost in each ($\text{NSIDE} = 2048$) HEALPix pixel from sub-pixel masking. Sub-pixel masking arises from two sources: foreground Galactic stars from Gaia, which will mask any unWISE source within $2.75''$ due to our Gaia point-source exclusion, and unWISE masking of diffraction spikes, latents and ghosts around bright stars⁷. We apply a binary mask to remove all pixels with more than 20% area lost due to sub-pixel masking, and we correct the density in the remaining pixels by dividing by the fractional unmasked area of each pixel.

We apodize the Planck lensing mask (with additional exclusion of $|b| < 10^\circ$) with a 1° FWHM Gaussian. We do not apodize the stellar, large galaxy, planetary nebulae or area lost masks. We use the apodized Planck lensing mask for the CMB lensing map and the product of the apodized lensing mask and the unapodized stellar, large galaxy, planetary nebulae and area-lost masks for the unWISE galaxy map. This yields $f_{\text{sky}} = 0.586$ for the unWISE galaxy map.

3 Model

3.1 Angular Clustering

Both the CMB lensing convergence κ and the unWISE projected galaxy density are projections of 3D density fields. We define the projection through kernels $W(\chi)$, where χ is the line-of-sight comoving distance. Given two such fields X, Y on the sky their angular cross-power spectrum is

$$C_\ell^{XY} = \frac{2}{\pi} \int_0^\infty d\chi_1 d\chi_2 W^X(\chi_1) W^Y(\chi_2) \int_0^\infty k^2 dk P_{XY}(k; z_1, z_2) j_\ell(k\chi_1) j_\ell(k\chi_2) \quad . \quad (3.1)$$

On small angular scales (high ℓ) one may make the Limber approximation [45], under which C_ℓ reduces to a single integral of the equal-time, real-space power spectrum:

$$C_\ell^{XY} = \int d\chi \frac{W^X(\chi) W^Y(\chi)}{\chi^2} P_{XY} \left(k_\perp = \frac{\ell + 1/2}{\chi}, k_z = 0 \right) \quad (3.2)$$

⁶<https://github.com/moustakas/LSLGA>

⁷http://catalog.unwise.me/files/unwise_bitmask_writeup-03Dec2018.pdf

where we have included the lowest order correction to the Limber approximation, $\ell \rightarrow \ell + 1/2$, to increase the accuracy to $\mathcal{O}(\ell^{-2})$ [46].

Lensing is sourced by the Weyl potential, which is related to the total matter power spectrum (including neutrinos) by the Poisson equation. Writing C_ℓ in terms of the galaxy-matter and matter-matter power spectra P_{mg} and P_{gg} , the weight functions $W(\chi)$ are

$$W^\kappa(\chi) = \frac{3}{2}(\Omega_m + \Omega_\nu)H_0^2(1+z) \frac{\chi(\chi_\star - \chi)}{\chi_\star} \quad , \quad W^g(\chi) = b(z)H(z) \frac{dN}{dz} \quad (3.3)$$

with χ_\star the distance to last scattering and $\int dz dN/dz = 1$.

Besides density-density and density-lensing correlations, there are also correlations induced by lensing magnification of background sources:

$$C_\ell^{\kappa g} \rightarrow C_\ell^{\kappa g} + C_\ell^{\kappa \mu} \quad (3.4)$$

$$C_\ell^{g_1 g_2} \rightarrow C_\ell^{g_1 g_2} + C_\ell^{g_1 \mu_2} + C_\ell^{g_2 \mu_1} + C_\ell^{\mu_1 \mu_2} \quad (3.5)$$

where

$$W^{\mu, i}(\chi) = (5s - 2) \frac{3}{2}(\Omega_m + \Omega_\nu)H_0^2(1+z)g_i(\chi) \quad (3.6)$$

$$g_i(\chi) = \int_\chi^{\chi_\star} d\chi' \frac{\chi(\chi' - \chi)}{\chi'} H(z') \frac{dN_i}{dz'} \quad (3.7)$$

where $s \equiv d \log_{10} N/dm$ is the response of the number density to a multiplicative change in brightness. Given our complex selection function, we measure the response by finite difference, artificially changing each magnitude by the same amount (in analogy to lensing magnification) and measuring the change in number of galaxies satisfying our selection criteria. This procedure is discussed in detail in Appendix C for both the unWISE galaxies (necessary for modeling the angular power spectra) and for the spectroscopic samples (necessary for determining magnification bias contamination to the clustering redshifts). For the color-selected unWISE samples, the response s may be significantly different from the slope of the luminosity function at the magnitude limit because the color cut is magnitude dependent.

3.2 HaloFit model

In order to compute C_ℓ we need to model $P_{\text{gg}}(k, z)$, $P_{\text{mg}}(k, z)$ and $P_{\text{mm}}(k, z)$. In this paper, we do not explore the cosmological implications of our measurement, but rather seek to characterize the unWISE samples and their redshift distribution, and present a measurement of the cross-correlations. For this purpose, a phenomenological fit will be sufficient, and we choose to model the auto and cross correlation in terms of a linear bias, multiplied by the ‘‘HaloFit’’ fitting function [47] to the non-linear matter power spectrum as implemented in the CLASS code [48]:

$$P_{\text{mg}}(k, z) = b_{\text{lin}}(z)P_{\text{mm}}(k, z) \quad , \quad P_{\text{gg}}(k, z) = b_{\text{lin}}^2(z)P_{\text{mm}}(k, z) + \text{Shot Noise} \quad (3.8)$$

This procedure has been shown to produce fairly reasonable phenomenological fits to the auto and cross correlations.⁸ While the fit may be good, ref. [49] has shown that the value of the inferred cosmological parameters can be significantly biased if HaloFit is used, and for this

⁸For the magnification bias terms, each ℓ maps to higher k than for the clustering terms; therefore the linear bias times HaloFit model is less adequate for $C_\ell^{\mu g}$. However, the magnification bias terms are subdominant compared to the clustering terms, so inaccuracy in modeling $C_\ell^{\mu g}$ is not significant.

reason we will explore a more sophisticated bias model to better model non-linearities in our cosmological analysis in ref. [26].

Since the galaxy field responds to dark matter and baryons only [50–54], P_{gg} is the power spectrum of non-neutrino density fluctuations. Although lensing responds to the power spectrum of total fluctuations, on the scales of interest here the neutrinos cause a scale-independent suppression of power. Therefore, using the non-neutrino power spectrum throughout and substituting $\Omega_m + \Omega_\nu \rightarrow \Omega_m$ greatly simplifies the modelling and makes less than 1% difference compared to the exact calculation.

4 Angular clustering

In this section we discuss our method of estimating the auto and cross spectra, as well as their covariance matrix.

4.1 Angular power spectra estimation

In order to estimate the binned cross and auto power spectra, we use a pseudo- C_ℓ estimator [55] based on the harmonic coefficients of the galaxy and lensing fields. The measured pseudo- C_ℓ on the cut sky are calculated as

$$\tilde{C}_\ell^{XY} = \frac{1}{2\ell + 1} \sum_m X_{\ell m} Y_{\ell m}^* \quad (4.1)$$

where $X, Y \in \{g_1, g_2, g_3, \kappa\}$ are the observed fields on the cut sky. Because of the mask, these differ from the true C_ℓ that are calculated from theory, but their expectation value is related through a mode-coupling matrix, $M_{\ell\ell'}$, such that

$$\langle \tilde{C}_\ell \rangle = \sum_{\ell'} M_{\ell\ell'} C_{\ell'} \quad (4.2)$$

The matrix $M_{\ell\ell'}$ is purely geometric and can be computed from the power spectrum of the mask itself. While Eq. (4.2) is not directly invertible for all ℓ , the MASTER algorithm [55] provides an efficient method to do so assuming that the power spectrum is piecewise constant in a number of discrete bins, b . Defining a “binned” mode-coupling matrix, $\mathcal{M}_{bb'}$ [56], we can recover unbiased binned bandpowers

$$C_b = \sum_{b'} \mathcal{M}_{bb'}^{-1} \tilde{C}_{b'} \quad . \quad (4.3)$$

We use the implementation in the code `NaMaster`⁹ [56]. Finally, the theory curve must be binned in the same way as the data when comparing theory and measurements. Since the true C_ℓ are not piecewise constant, this involves the following steps [56]: First, the theory curve is convolved with $M_{\ell\ell'}$ using Eq. (4.2). Then the convolved theory, $\tilde{C}_\ell^{\text{theory}}$, is binned in the same bins, b , as the data to form bandpowers, $\tilde{C}_b^{\text{theory}}$, and finally the bandpowers are decoupled using Eq. (4.3) to obtain C_b^{theory} . While for simplicity the plots show unbinned theory curves, all of the calculations are performed with binned quantities.

In short, our pipeline works as follows: first, we mask the Planck lensing map with the mask provided by the Planck team, apodized with a Gaussian smoothing kernel with FWHM

⁹<https://github.com/LSSTDESC/NaMaster>

1 deg. For the unWISE galaxies, we use the custom-made mask described in Section 2.4, which includes different apodization schemes for the wide Galactic mask and point sources. In addition, we have to consider that Galactic stars can mask galaxies behind them or in their vicinity, a problem that becomes more severe closer to the galactic plane. To correct for this, we create an “area lost” mask (described in Section 2.4) and divide the observed galaxy number count by the area available in each pixel, to obtain an unbiased estimate of the local number of galaxies. Then a galaxy overdensity field is created, and cross-correlated with the CMB lensing maps using **NaMaster**. Finally, we need to correct for the pixel window function, due to the assignment of galaxies to discrete pixels: we divide C_ℓ^{kg} by the HEALPix pixel window function at the center of each bandpower. The procedure is more complicated for C_ℓ^{gg} : a shot-noise power spectrum has correlation length zero and thus does not need to be corrected for the pixel window function, whereas the signal part of C_ℓ^{gg} should be divided by the square of the pixel window function. Therefore, we first subtract the estimated shot noise from C_ℓ^{gg} using \bar{n} from Table 1, then divide by the squared pixel window function, and then add the estimated shot noise back.

We tested this pipeline on Gaussian realizations of the CMB lensing and galaxy fields, and noted that the final “deconvolved” C_ℓ are rather sensitive to the choice of apodization scale, especially for the CMB lensing map, but are not affected by the inclusion of unapodized components in the galaxy mask. Our choice of smoothing was determined by optimizing the recovered power spectrum in simulations with known input angular correlation. In particular, we use the above **NaMaster** pipeline to measure C_ℓ for 100 simulated Gaussian lensing and galaxy maps (generated with the correct cross-correlation). We find significant biases of several percent due to power leakage outside the measured range, if the $\ell_{\max}^{\text{NaMaster}}$ used in **NaMaster** is close to the $\ell_{\max} = 1000$ used in our analysis. To remedy this, we run **NaMaster** with $\ell_{\max}^{\text{NaMaster}} = 6000$, before extracting the bandpowers in our analysis range and discarding the higher ℓ ones.

With the Gaussian simulations, we also find biases of several percent in the recovery of the galaxy auto-spectrum at $\ell < 300$ (Figure 2). Mask-induced mode coupling causes $\ell < 50$ systematic power in the auto-spectrum to leak to considerably higher ℓ . We find that if we turn off the extra low- ℓ power by using the theory prediction rather than the measured C_ℓ^{gg} as the input power spectrum, we can recover C_ℓ^{gg} with no bias.

We therefore filter all modes with $\ell < 20$ in the unmasked galaxy map. To do this, we take the spherical harmonic transform of the raw galaxy map (before applying the mask), apply a sharp cut setting all modes with $\ell < 20$ to zero, and apply the inverse transform to recover the filtered map. We then use the filtered map as input for our **NaMaster** pipeline. We find this procedure leads to considerably less biased recovery of the auto-spectrum (Figure 2). Other approaches (i.e. setting the edge of the smallest- ℓ bin to $\ell_{\min}^{\text{NaMaster}} = 20$ or filtering $\ell < 50$ modes instead) also recover the unbiased auto and cross-spectra. We correct the auto-spectra for the residual mask-transfer bias. Since the residual bias is $\leq 1\%$, smaller than the statistical errors on the cross spectrum or the statistical errors from uncertain dN/dz , this correction has only a small impact on our results (compare the “no transfer function” row to the fiducial row in Figure 12).

We conclude that with our pipeline we can measure all of the auto and cross-correlations between the different samples with sub-percent accuracy over the whole range of scales considered, once the input maps have been filtered and the mask-deconvolution transfer function has been applied.

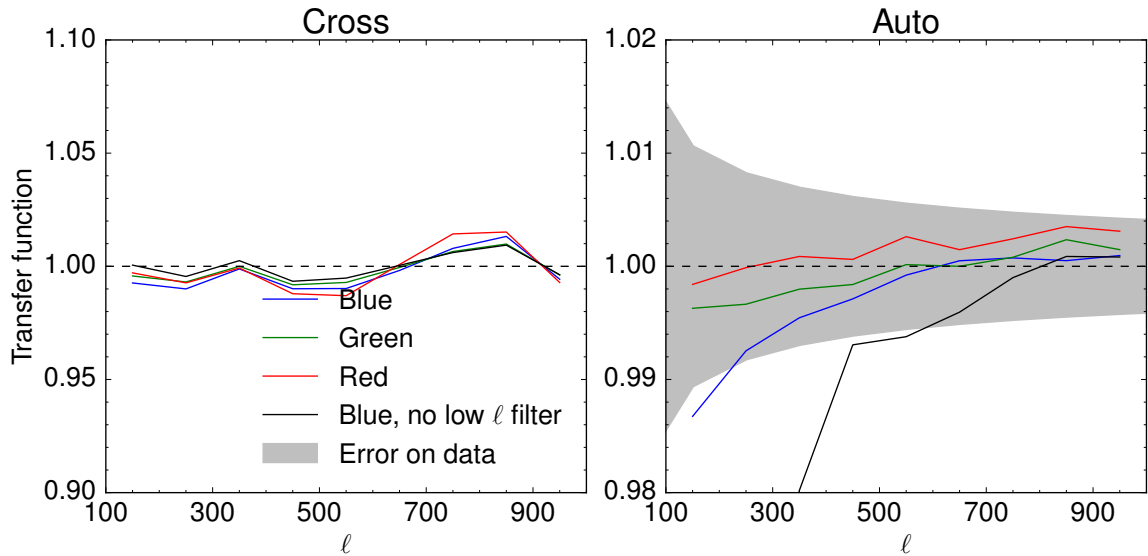


Figure 2. Mask deconvolution transfer function for the CMB lensing cross-spectra (left) and galaxy auto-spectra (right), i.e. comparison between input power spectrum and output after masking, pseudo- C_ℓ estimation, and mask deconvolution. Maps were generated from power spectra assuming a Gaussian field. Colored curves are transfer functions for different samples after filtering $\ell < 20$ modes from the unmasked map, whereas no filtering was applied to black curves. Recovery of the cross-spectrum is unbiased even without filtering, but recovery of the auto-spectrum requires filtering $\ell < 20$ modes. To ensure sub-percent accuracy, we additionally correct the auto-spectrum by the transfer function displayed here.

4.2 Covariance matrix

While an exact computation of the covariance matrix after applying the MASTER algorithm for a Gaussian random field is possible, it is computationally very demanding, involving $\mathcal{O}(\ell_{\text{max}}^6)$ operations. Refs. [57, 58] have proposed an approximate method to estimate the Gaussian part of the covariance matrix that makes it as computationally expensive as the power spectrum itself. This procedure has been validated on simulations and shown to work extremely well [58]. This algorithm is implemented in `NaMaster`, and takes as input the true auto and cross spectra (for example, from the theory curves with the correct value of parameters including the galaxy bias). Since measuring the bias requires a covariance matrix to start with, an iterative approach may be used. For computational simplicity, we adopt a further approximation which will assume the decoupled covariance matrix to be diagonal, and where the on-diagonal elements for binned bandpowers of width $\Delta\ell$ are given by [55]:

$$\text{Cov}(C_\ell^{XY}, C_{\ell'}^{XY}) = \sigma^2(C_\ell^{XY})\delta_{\ell,\ell'} = \frac{[C_\ell^{XX}C_\ell^{YY} + (C_\ell^{XY})^2]_{\text{measured}}}{f_{\text{sky}}(2\ell + 1)\Delta\ell} \frac{w_4}{w_2} \delta_{\ell,\ell'} \quad (4.4)$$

Here the weights w_2 and w_4 are defined in terms of the arbitrary mask weights $W(\hat{\mathbf{n}})$ as:

$$w_i f_{\text{sky}} = \frac{1}{4\pi} \int_{4\pi} d\Omega_{\hat{\mathbf{n}}} W^i(\hat{\mathbf{n}}) \quad (4.5)$$

with $w_1 f_{\text{sky}} = f_{\text{sky}}$. If $X \neq Y$ and the fields have different masks, we take w_2 and w_4 to be the geometric means of the ones computed with each of the individual masks.

Using the method for analytic Gaussian pseudo- C_ℓ covariance in refs. [57, 58], we have checked that the largest off-diagonal correlation between bandpowers is 4% for the two lowest ℓ bins, and that the on-diagonal elements agree to percent level. Therefore we conclude that the approximation in Equation 4.4 is adequate for our purposes. Furthermore, we neglect any non-Gaussian contribution to the covariance matrix, since we will only model scales that are in the linear or mildly non-linear regimes, where these corrections are expected to be small.

5 Galaxy redshift distribution

Since the unWISE galaxy sample is selected from two-band imaging, dN/dz cannot be determined by photometric redshifts. We instead measure dN/dz using cross-correlations with large-area spectroscopic surveys [59–61], supplemented by redshifts from cross-matching to deep multi-band photometry in a small field. Cross-correlation redshifts measure $b(z)dN/dz$ (in the absence of a small contribution from magnification bias), which is the relevant kernel for modeling $C_\ell^{\kappa g}$ and C_ℓ^{gg} (Section 3). Therefore, unlike previous work, we are not concerned with disentangling dN/dz from the bias evolution of the unWISE galaxies. $C_\ell^{\kappa g}$ and C_ℓ^{gg} do contain a subdominant contribution from magnification bias, which depends on dN/dz alone; in this context, we use dN/dz measured from cross matches to the COSMOS photometric catalog. Consistency between the cross-match dN/dz and cross-correlation $b(z)dN/dz$ requires that the bias increase strongly with redshift. In Appendix B, we show that a simple halo occupation distribution of the unWISE galaxies exhibits a similar increase in bias, demonstrating that our approach is self-consistent.

In Sections 5.1 and 5.2 we describe our methodology for measuring the cross-correlation and cross-match redshifts and estimating their uncertainties, which constitute a substantial portion of the error budget in modeling the angular power spectra. In Figure 3 we list the steps outlined in Sections 5 and 6 to interpret the clustering of the unWISE samples: estimate the redshift distribution, determine the best-fit linear bias of each sample, and estimate the uncertainty on the bias due to uncertain redshift distribution. Throughout Sections 5 and 7, we quantify systematic errors in terms of their impact on the best-fit bias to the CMB cross ($C_\ell^{\kappa g}$) and galaxy auto power spectra (C_ℓ^{gg}) of the unWISE samples.

5.1 Cross-match redshifts

One estimate of dN/dz can be obtained by matching the unWISE samples to deep catalogs with photometric redshifts. The deepest sample of well-measured photometric redshifts comes from the COSMOS field, where deep photometry in many bands spanning the ultraviolet through infrared allows precise photometric redshifts for all sources detected by WISE with $\Delta z/(1+z) = 0.007$ [41]. We first trim the COSMOS catalog to include only objects brighter than 20.7 (19.2) Vega mag at 3.6 (4.2) μm . These depths are roughly 2.5 mag fainter than the 50% completeness limit for the unWISE catalog [17], so excluding fainter objects removes no objects that WISE could conceivably detect. We then match COSMOS sources to unWISE sources at a radius of 2.75'' over the 2 deg² overlap, considering the closest COSMOS source within 2.75'' to be the true match.

The COSMOS catalog marks many bright stars as galaxies, so we additionally edit the COSMOS catalog so that bright objects which Gaia identifies as pointlike are classified as stars, as long as those objects are not X-ray selected. We find that stellar contamination of

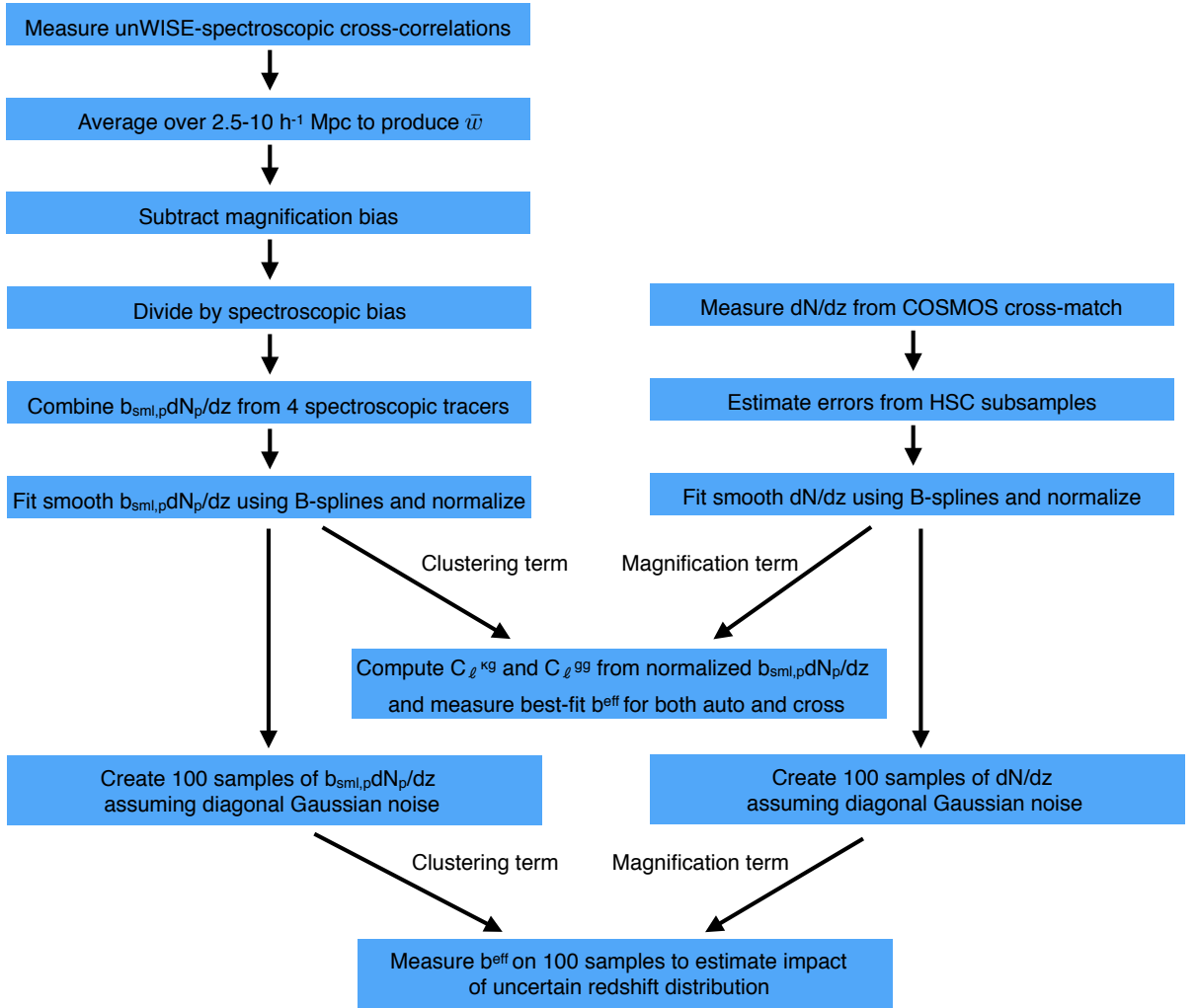


Figure 3. An outline of the steps required to interpret the angular clustering of the unWISE samples: estimate the redshift distribution, fit a linear bias to C_ℓ^{kg} and C_ℓ^{gg} , and estimate the impact of uncertainty in the redshift distribution on the fitted biases.

the unWISE samples is very low, with 1.8%, 1.6%, and likely $< 1\%$ ¹⁰ of the blue, green and red samples classified as stars.

For each source, we use the redshift corresponding to the median of the likelihood distribution (“photoz” in the COSMOS catalog). If the SED is better fit by an AGN template than a galaxy template, we instead use the redshift from the AGN template fit (“zq” in the catalog); we find 19%, 30% and 41% of the blue, green and red sample are classified as AGN by this criterion. However, for these objects “zq” and “photoz” are very similar.

Due to the small area of the COSMOS field, sample variance can be larger than the Poisson variance on dN/dz . We therefore estimate uncertainty on dN/dz by constructing 44 subsamples, each of $\sim 2 \text{ deg}^2$, from the HSC SSP survey [62, 63]. Compared to COSMOS,

¹⁰The red sample only has 188 matches to the COSMOS photometric catalog and none of them are stars; the error on the stellar contamination fraction may therefore be quite large. For the fainter red samples reaching to $W2 = 16.5$ or 16.7 , we find stellar contamination of 0.6% and 0.8%, respectively.

Color	Median z (b -weighted)	Std	Percentile (5%-95%)	Median z $\ell < 155^\circ$	Median z $\ell > 155^\circ$	Median z	Std	Percentile (5%-95%)
Blue	0.72	0.031	0.11	0.75	0.72	0.63	0.022	0.06
Green	1.38	0.026	0.09	1.35	1.38	1.09	0.019	0.06
Red	1.70	0.064	0.23	1.71	1.68	1.46	0.030	0.09

Table 2. Summary statistics of the redshift distribution of the WISE sample. Statistics on the left are computed from samples of $b_{\text{sml,p}}dN_p/dz$ (i.e. clustering redshifts), while statistics on the right are computed from samples of the cross-match dN/dz . Std gives the standard deviation of the medians of the 100 dN/dz samples. Galactic longitude 155° approximately splits the sky in half, so the $\ell = 155^\circ$ split provides another estimate of the uncertainty on the clustering redshifts.

HSC is slightly shallower but covers a much larger area ($\sim 120 \text{ deg}^2$). However, the HSC photometric redshifts are less accurate than COSMOS and become biased at $z > 1.5$,¹¹ where a substantial fraction of galaxies scatter to $z_{\text{HSC}} \sim 1$, biasing dN/dz_{HSC} at $z \geq 1$ compared to dN/dz_{COSMOS} . As a result, we restrict the HSC comparison to $z < 1$. We use the DEmP photometric redshifts, as these are the most accurate redshifts available for all “primary” HSC objects [63]. We require that the HSC objects have clean photometry: we only use “primary” sources, and remove sources with pixel flags indicating saturated or interpolated pixels, bad pixels, cosmic ray hits, suspect and clipped pixels, and poor centroid measurements. We also require that the objects are classified as extended sources or have $i > 23$, where the star-galaxy classification performs poorly. As with COSMOS, we use the closest match within $2.75''$.

We find that the dN/dz errors are larger than Poisson statistics would indicate, by roughly redshift-independent factors of 3.8, 1.9 and 1.1 for the blue, green and red samples at $z < 1$. Since we cannot use HSC to determine dN/dz errors at $z > 1$, where the DEmP photometric redshifts become significantly biased, we extrapolate the dN/dz uncertainty to higher redshift by multiplying the Poisson error bars by a constant factor of 3.8, 1.9 and 1.1 for blue, green and red samples. This extrapolation yields error bars appropriate for the cosmic variance contribution alone; in Section 7.4 we discuss the impact of photometric redshift errors on dN/dz and on our bias results.

We give summary statistics for the cross-match dN/dz in Table 2 and plot the cross-match dN/dz in Figure 7. Even at low redshift, there is a systematic shift between the COSMOS and HSC dN/dz for the red sample; this may be due to errors in the $z < 1$ HSC redshifts. The impact of this shift is limited because the cross-match dN/dz is only used to model the magnification bias term. Therefore, even the $\Delta z = 0.3$ shift required to reconcile the COSMOS and HSC dN/dz for the red sample makes $\lesssim 0.7\sigma$ difference on the bias fitted to the auto and cross-correlation.

5.2 Cross-correlation redshifts

Another method for determining dN/dz is through cross-correlation with a spectroscopic sample. This is an old method has been revived in several recent works [59–61, 64–75] (including validation against spectroscopic redshifts in ref. [66]), but here we present one of its first applications to modeling galaxy power spectra. We therefore discuss and quantify

¹¹See page A5 in https://hsc-release.mtk.nao.ac.jp/doc/wp-content/uploads/2017/02/s16a_demp_median.pdf, which plots bias, scatter, and outlier fraction as a function of reference redshift for the training set used by HSC.

several sources of systematic error, including nonlinear clustering and nonlinear bias evolution; magnification bias contribution to the photometric-spectroscopic cross-correlation; and bias evolution of the various spectroscopic samples as required to combine cross-correlations with multiple spectroscopic samples.

In the Limber approximation the cross-correlation of a photometric survey with scale-independent bias $b_{\text{sml,p}}(z)$ and redshift distribution dN_{p}/dz , and a spectroscopic survey with bias $b_{\text{sml,s}}(z)$, in a narrow bin between z_{min} and z_{max} is

$$C_{\ell}^{\text{p-s cross}} = b_{\text{sml,s}}(z) b_{\text{sml,p}}(z) H(z) \frac{dN_{\text{p}}}{dz} \int_{z_{\text{min}}}^{z_{\text{max}}} dz \frac{dN_{\text{s}}}{dz} \frac{P_{\text{mm}}(k = (\ell + \frac{1}{2})/\chi, z)}{\chi^2} + C_{\ell}^{\text{mag}} \quad (5.1)$$

where C_{ℓ}^{mag} includes the contributions from the three lensing magnification bias terms; we assume the bin is sufficiently narrow that the biases and $dN_{\text{p}}/d\chi$ are constant across the bin; and both biases are assumed to be scale-independent.

We refer to the biases here as b_{sml} to emphasize that they are defined on relatively small scales ($2.5 - 10 h^{-1}$ Mpc) on which we measure the spectroscopic-photometric cross-correlations. This is in contrast to the large-scale bias, b_{lin} , relevant to the modeling of the angular power spectrum in Section 3. However, as discussed below and in Section 7, b_{sml} and b_{lin} are within 15% of each other for all of the unWISE samples, and the systematic error from the discrepancy between b_{sml} and b_{lin} is subdominant to the statistical error from uncertainty in $b dN/dz$.

We have implemented a cross-correlation dN/dz estimate in both harmonic and configuration space, obtaining consistent results. It is convenient, and consistent with past results, to first present the spectroscopic-photometric cross-correlations in configuration space. We use the estimator of Ref. [61], in which the correlation function is weighted by r^{-1} to increase the signal-to-noise ratio and integrated over a range of scales:

$$\bar{w}_{\text{sp}}(z) = \sum_i r_i^{-1} \Delta r_i w_{\text{sp,binned}}(r_i, z) \quad (5.2)$$

where we use three log-spaced bins in r between 2.5 and $10 h^{-1}$ Mpc. The binned correlation function is given by

$$w_{\text{sp,binned}}(r_i, z) = \int \frac{\ell d\ell}{2\pi} C_{\ell}^{\text{p-s cross}} \frac{1}{\pi(r_{\text{max},i}^2 - r_{\text{min},i}^2)} \int_{r_{\text{min},i}}^{r_{\text{max},i}} 2\pi r dr J_0(\ell\theta) \quad (5.3)$$

Noticing that $\theta = r/\chi$ ¹² and switching integration variables from ℓ to k we can write

$$\bar{w}_{\text{sp}}(z) = b_{\text{sml,s}}(z) b_{\text{sml,p}}(z) H(z) \frac{dN_{\text{p}}}{dz} I(z) + \bar{w}_{\text{mag}}(z) \quad (5.4)$$

with

$$I(z) = \int \frac{k dk}{2\pi} \int_{z_{\text{min}}}^{z_{\text{max}}} dz \frac{dN_{\text{s}}}{dz} P_{\text{mm}}(k, z) \sum_{r_i} \frac{r_i^{-1} \Delta r_i}{\pi r_{\text{max},i}^2 - \pi r_{\text{min},i}^2} \int_{r_{\text{min},i}}^{r_{\text{max},i}} 2\pi r J_0(kr) dr \quad (5.5)$$

¹² When measuring $w(\theta)$, we count pairs in angular bins with $\theta_i = r_i/\chi_{\text{central}}$, where χ_{central} is the comoving distance to the center of the sub-bin. Therefore, within each sub-bin, $r = \theta\chi_{\text{central}}$, which is well approximated by $r = \theta\chi$ because the sub-bins are narrow. This simplifies the triple integral in Equation 5.5 by allowing the r integral to be redshift-independent.

In the linear regime $I(z)$ is equal to $D^2(z)$ times a redshift-independent integral, which is degenerate with the normalization of dN_p/dz . On our scales of interest, $I(z)$ deviates only slightly from $D^2(z)$ ($\sim 5\%$ at $z = 2$). To compute $I(z)$ we use the HaloFit nonlinear matter power spectrum from Ref. [76] for $P_{\text{mm}}(k, z)$ and continue to assume scale-independent bias. While the $I(z)$ term introduces a cosmology dependence into the clustering redshifts, normalizing the clustering redshifts eliminates the relationship between redshift distribution and power spectrum amplitude, allowing us to constrain the power spectrum amplitude (i.e. $\sigma_8(z)$) averaged over the redshift distribution of each unWISE sample.

Lensing magnification can correlate samples widely separated in redshift and therefore bias clustering redshifts in the tails of the distribution [60, 74]. We estimate the contribution of magnification bias $\bar{w}_{\text{mag}}(z)$ using the COSMOS cross-match dN/dz and the measured s for unWISE and the spectroscopic samples (Appendix C), and assuming a scale-independent bias times the HaloFit power spectrum. We use the following form for the bias evolution of each sample:

$$b_{\text{sml,p}}(z) = 0.8 + 1.2z \quad \text{Blue} \quad (5.6a)$$

$$b_{\text{sml,p}}(z) = \max(1.6z^2, 1) \quad \text{Green} \quad (5.6b)$$

$$b_{\text{sml,p}}(z) = \max(2z^{1.5}, 1) \quad \text{Red} \quad (5.6c)$$

with $\max(a, b)$ meaning the larger of a and b . This form is roughly consistent both with the observed clustering given the cross-match dN/dz and the expected bias evolution from a simple HOD of the unWISE samples (Figure 19). Since the unWISE bias evolution is only required to model the magnification bias correction to the cross-correlation redshifts, more quantitative agreement with the observed clustering is not needed. If we instead use $b_{\text{sml,p}}(z)$ from the cross-correlation redshifts after the initial magnification bias correction, the bias fitted to $C_\ell^{\kappa g}$ and C_ℓ^{gg} changes by $< 0.4\sigma$.

We show \bar{w} and the magnification bias correction in Figure 5. Magnification bias has the largest impact on the blue sample, with CMASS galaxies at $z > 0.6$ showing the largest impacts.

We can invert Equation 5.4 to derive $b_{\text{p,sml}}dN_p/dz$ given a measurement of \bar{w}_{sp} . We measure the binned correlation function using the estimator of ref. [77]

$$\hat{w}_{\text{sp,binned}}(\theta) = \frac{D_s D_p}{D_s R_p} \frac{N_R}{N_D} - 1 \quad (5.7)$$

using three log-spaced bins between¹³ 2.5 and 10 h^{-1} Mpc, with the inner radius set to reduce the contributions from scale-dependent bias and “1-halo” effects. Since the unWISE galaxy density varies across the sky (slightly decreasing towards the Galactic center), we measure the normalization $N_R/N_D(\theta)$ in NSIDE = 8 HEALPix pixels. If the annulus in which we count pair straddles two NSIDE = 8 pixels, we average the normalization in the two pixels. Our correlation function code is publicly available at <https://github.com/akrolewski/BallTreeXcorrZ> and has been tested to ensure that the correlation function as measured on the curved sky is correct.

¹³At all redshifts, the lower limit corresponds to much larger angular scales than those affected by the WISE PSF and suppression by nearby bright sources; see Fig. 25 in http://wise2.ipac.caltech.edu/docs/release/allsky/expsup/sec6_2.html#brt_stars for estimation of this scale.

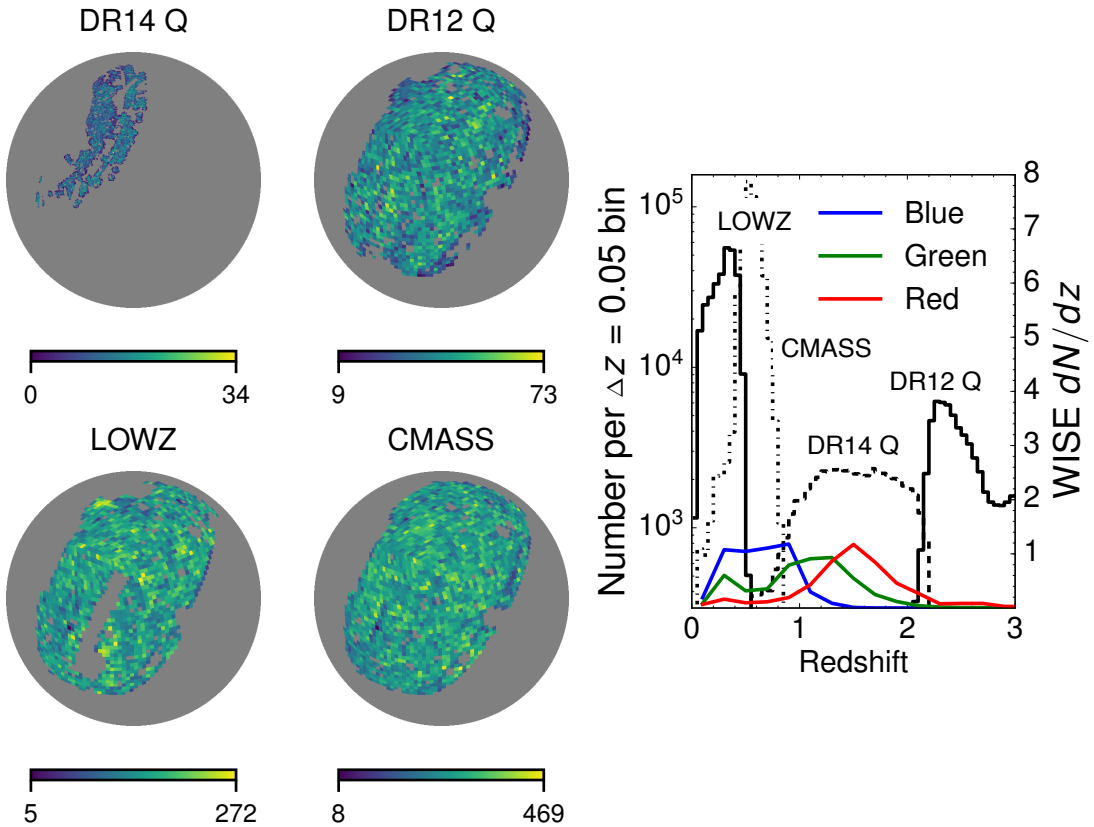


Figure 4. *Left:* Sky maps of spectroscopic samples used for cross-correlation redshifts in Galactic coordinates. *Right:* Redshift distributions of spectroscopic samples (black curves) used for cross-correlation redshifts. unWISE galaxy distributions (colored curves) are overplotted with arbitrary amplitude.

We cross-correlate the unWISE photometric galaxies with spectroscopic quasars from BOSS DR12 [78] and eBOSS DR14 [79]¹⁴ and galaxies from BOSS CMASS and LOWZ [80]. We plot the redshift and sky distributions of the spectroscopic samples used for the clustering redshifts in Figure 4.

We split the spectroscopic samples into bins of width $\Delta z = 0.05$ at $z < 0.8$ and $\Delta z = 0.2$ at $z > 0.8$ where the errorbars become much larger due to the sparser quasar samples. As Δz becomes narrower, the signal-to-noise in each individual bin decreases, but the total signal-to-noise of dN/dz increases modestly (by $\sim 35\%$ as Δz changes from 0.1 to 0.02). We prefer having a relatively high signal-to-noise in the individual bins, particularly at high redshift where dN/dz is nearly zero but our errorbars are also relatively large.

We restrict the BOSS quasars to the “CORE”-like sample from ref. [81] (similar to the “QSO_CORE_MAIN” targeting flag, but only including quasars that would have been selected by the XDQSO method [82],¹⁵ and removing quasars lying in regions where the targeting

¹⁴While the BOSS and SDSS quasar catalogs are independent, eBOSS includes previously observed quasars. We remove these quasars to create an independent sample; they comprise 45% of the northern eBOSS catalog.

¹⁵<https://xdqso.readthedocs.io/en/latest/>

Sample	z_{\min}	z_{\max}	N	Jackknife regions	Area (deg ²)
DR14 Q	0.8	2.2	54708	29	1178
DR12 Q	2.0	4.0	67175	34	6030
LOWZ	0.0	0.5	273549	31	5656
CMASS	0.1	0.8	544308	37	6670

Table 3. Properties of the spectroscopic samples used for cross-correlation redshifts.

completeness is $< 75\%$), as was done in previous quasar clustering analyses [81, 83]. We remove all objects in the southern galactic cap (SGC), which are a small fraction of the total spectroscopic sample. Differences in photometric calibration between the SGC and NGC lead to slightly different galaxy samples [84, 85], unexplained differences in quasar clustering between NGC and SGC [81, 83, 86], and differences in \hat{w}_{sp} , possibly resulting from the different spectroscopic bias evolution. We remove DR12 quasars at $z < 2$, DR14 quasars at $z > 2.2$, and DR14 quasars at $z < 0.8$, since these objects are outliers with redshifts different from each survey’s target redshift range and thus may have different clustering properties than the sample as a whole (indeed, we find somewhat discrepant measurements of \bar{w}_{sp} when comparing to BOSS and eBOSS quasars outside their primary redshift ranges). We also remove CMASS galaxies at $z > 0.8$ and $z < 0.1$ and LOWZ galaxies at $z > 0.5$, where the spectroscopic samples become too sparse to measure $b_{\text{sml,s}}$ (see below). We summarize the key properties of these samples in Table 3.

We apply the corresponding spectroscopic mask to each sample. For eBOSS we use the BOSS veto masks [80], pixelized to $\text{NSIDE} = 256$ HEALPix pixels, and we also mask $\text{NSIDE} = 128$ pixels where more than 80% of eBOSS quasars are in DR7 or DR12. For DR12 quasars, we apply the BOSS veto masks [80] and remove $\text{NSIDE} = 256$ pixels with $< 75\%$ completeness as computed from the BOSSQSOMASK software¹⁶ [81, 83]. For CMASS and LOWZ we use the corresponding BOSS DR12 LSS catalog masks.¹⁷ We also apply the same WISE masks that we use for the cross-correlation analysis. For the spectroscopic cross-correlations, we threshold all masks by setting pixels with mask value < 0.9 to zero and > 0.9 to one.

We use jackknife¹⁸ resampling to estimate errors on \bar{w}_{sp} . We start by splitting the sky into $\text{NSIDE} = 4$ HEALPix pixels¹⁹ and then combine neighboring pixels until the unmasked area within each region reaches a threshold, which we vary between 80 and 120% of the maximum pixel area, choosing the threshold that minimizes the difference between the largest

¹⁶<http://faraday.uwo.edu/~admyers/bossqsomask/>

¹⁷<https://data.sdss.org/sas/dr12/boss/lss/>

¹⁸We also investigated bootstrap resampling to estimate the covariance matrix of $w(\theta)$, and found that on scales smaller than the resampling pixel size (which is always larger than θ_{max}), jackknife errors agree well with errors from the “marked bootstrap” of Refs. [87, 88]. We prefer jackknife errors to bootstrap errors because sampling a pixel more than once double-counts all pairs in that pixel and is not a reasonable physical situation. Moreover, it leads to ambiguities in the situation where a spectroscopic source lies in pixel i and a photometric source lies in pixel j . In a naive implementation of the bootstrap, intra-pixel pairs are resampled $0, 1, 2, \dots, N$ times while cross-pixel pairs are resampled $0, 1, 4, \dots, N \times M$ times, leading to larger variance on all scales than jackknife or marked bootstrap. The marked bootstrap avoids this issue by resampling only one of the tracers. We also find very little difference between leave-one-out jackknife resampling and leave-two-out jackknife, so we opt for leave-one-out jackknife in the interest of simplicity.

¹⁹We use $\text{NSIDE} = 8$ pixels for the smaller-area eBOSS samples. We find that using too small pixels can underestimate the errorbars (as argued in ref. [89]), so we set the size of the resampling pixels so that ~ 30 are available for each sample.

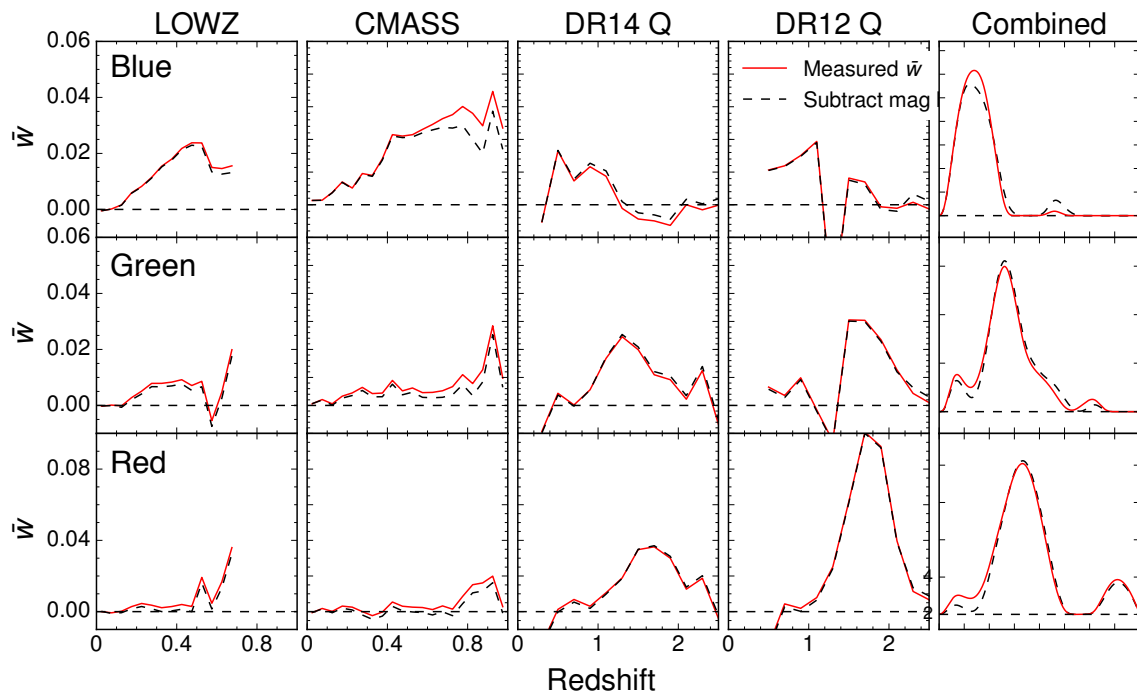


Figure 5. Measured \bar{w} without (black dashed) and with (red solid) magnification bias subtracted for unWISE galaxies crossed with our spectroscopic samples (labeled above each column), and for all samples combined (right-most panel).

and smallest regions. We list the number of regions used for each sample in Table 3. The error on \bar{w}_{sp} is then

$$\sigma_{\bar{w}}^2(z) = \sum_{L=1}^N \frac{R_{[L]}}{R} (\bar{w}_{[L]}(z) - \langle \bar{w}(z) \rangle)^2 \quad (5.8)$$

where R refers to the number of randoms, the subscript $[L]$ indicates that we exclude the L th region, and $\langle \bar{w}(z) \rangle$ is the average over all N jackknife resamples $\bar{w}_{[L]}(z)$. The replacement of the conventional factor $(N-1)/N$ with $R_{[L]}/R$ is an empirical correction for the fact that the regions have different areas (equation 5 in ref. [90]).

Combining multiple spectroscopic tracers (as is necessary in our case, due to the broad dN/dz of the unWISE samples) requires a measurement of $b_{\text{sml},s}(z)$. We measure $b_{\text{sml},s}(z)$ by fitting a scale-independent bias times Halofit to the measured $w(\theta)$ between 2.5 and 10 h^{-1} Mpc:

$$w_{\text{auto},s}(\theta, z) = b_{\text{sml},s}^2(z) \int_0^\infty k dk P_{\text{mm}}(k) \int_{\chi_{\text{min}}}^{\chi_{\text{max}}} \frac{d\chi}{2\pi} J_0(k\chi\theta) \left(\frac{dN_s}{d\chi} \right)^2 \quad (5.9)$$

where the integral over χ ranges between the lower and upper boundaries of each redshift bin. We omit SDSS DR7 quasars from our spectroscopic samples due to their poorly measured autocorrelation [91]. For BOSS galaxies and eBOSS quasars we use publicly available galaxy and random catalogs,²⁰ and for DR12 quasars we generate randoms using BOSSQSOMASK.

²⁰<https://data.sdss.org/sas/dr12/boass/lss/> for BOSS and <https://data.sdss.org/sas/dr14/eboass/lss/catalogs/> for eBOSS.

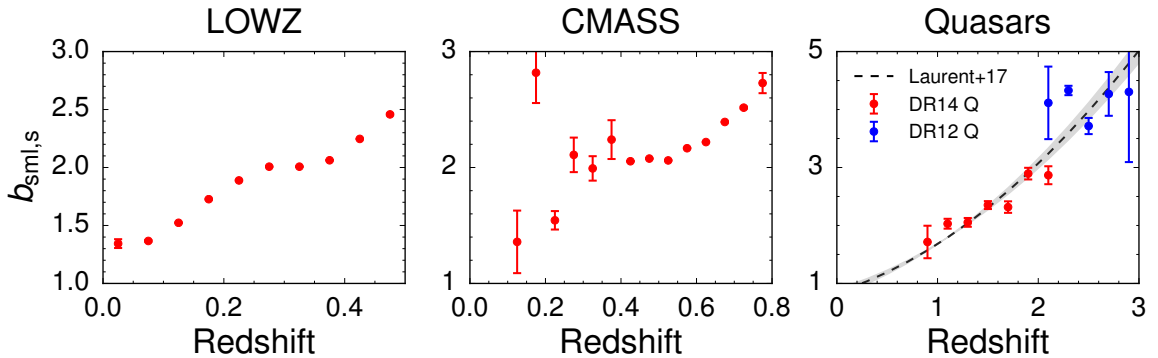


Figure 6. Measured bias, $b_{\text{sml},s}$, of spectroscopic samples as a function of redshift. The dashed line in the right panel corresponds to the fit from ref. [94] (with the gray band giving uncertainty in the fit). See Table 7 for a tabulated compilation.

For BOSS galaxies and eBOSS quasars we weight each object by the combined angular systematics, fiber collision and redshift failure weight (Equation 50 in ref. [80]), and for BOSS quasars we weight by the inverse of the targeting completeness [81, 83]. Note that the 55'' SDSS fiber collision radius is smaller than our inner bin of $2.5 h^{-1}\text{Mpc}$ at all redshifts that we consider. Previous work has shown that application of these systematics weights allows unbiased recovery of the correct cosmological clustering [81, 85, 92–94].

While previous measurements of the clustering exist for all spectroscopic samples, measurements for BOSS galaxies have generally been made in coarse redshift bins over a somewhat restricted redshift range ($0.2 < z < 0.6$) [95–97], so we use our measured bias values (Figure 6 and Table 7) to ensure that the scales used and redshift bins are consistent with the clustering redshifts. We check our results by replacing our BOSS galaxy spectroscopic bias measurements with those from Figure 12 in ref. [98] (who measure the bias in similar redshift bins, to measure clustering redshift distributions for Galactic dust maps), and find this makes $\lesssim 0.1\sigma$ difference in the bias fitted to C_ℓ^{gg} and $C_\ell^{\kappa g}$. We also propagate the fitting error on the spectroscopic bias to our clustering dN/dz measurement, although this is almost always subdominant to the statistical error on the cross-correlation.

For quasars, we find that the fitting function of ref. [94] provides a very good approximation to the measured bias evolution:

$$b_{\text{sml},s}(z) = (0.278 \pm 0.018) \left[(1+z)^2 - 6.565 \right] + (2.393 \pm 0.042) \quad (5.10)$$

Once we have measured the spectroscopic bias, we can divide \bar{w} by $b_{\text{sml},s}$ (as in equation 5.4) to obtain dN_p/dz for each spectroscopic tracer (quasars, CMASS and LOWZ galaxies). We then combine dN_p/dz for the different tracers by inverse-variance weighting in each redshift bin. We find good agreement between the clustering redshift measurements from CMASS and LOWZ in the redshift range where they overlap ($0 < z < 0.5$) with $\chi^2 = 12.1$ over 10 dof (7.7/10, 2.8/10) for the blue (green, red) samples. We plot the final redshift distributions in Fig. 7, along with samples drawn from the uncertainty in the redshift distribution.

To model the angular power spectra, the redshift distribution must satisfy physical constraints ($b_{\text{sml},p}dN_p/dz > 0$ and $b_{\text{sml},p}dN_p/dz|_{z=0} = 0$)²¹ and have well-characterized un-

²¹The number of galaxies per area per comoving distance, $dN/d\chi$, is related to the comoving number density \bar{n} as $dN/d\chi(\chi) = \bar{n}4\pi\chi^2$ so at $\chi = 0$, $dN/d\chi$ and therefore dN/dz must go to zero.

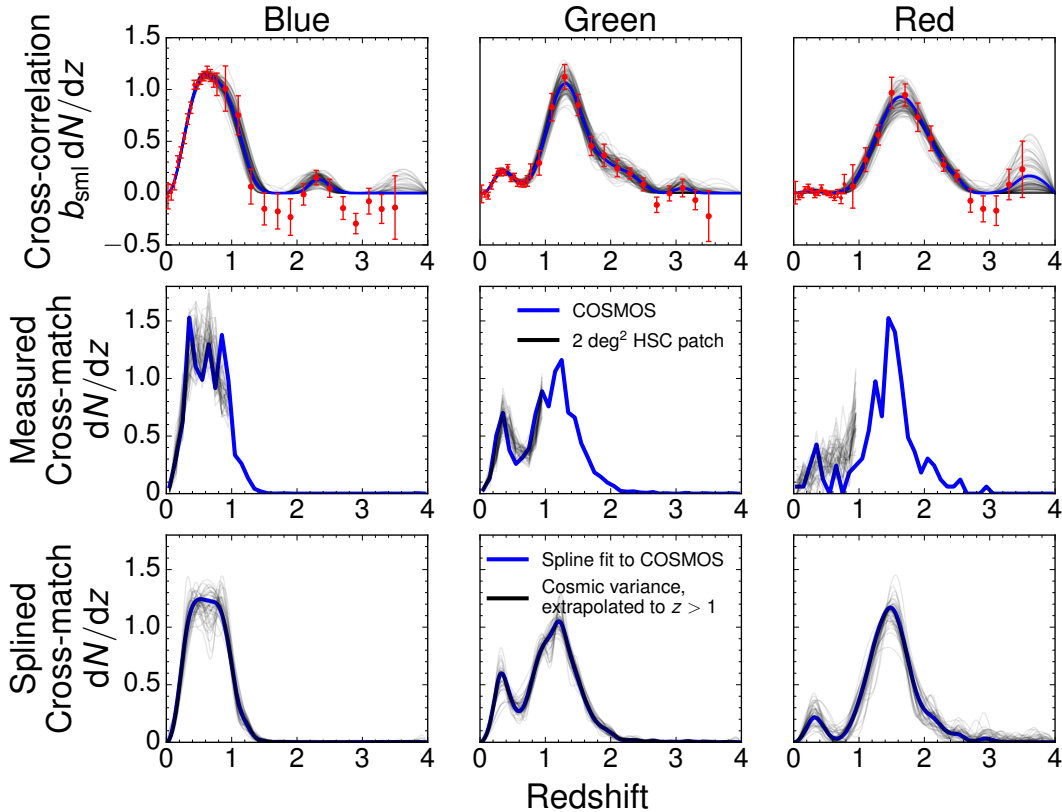


Figure 7. *Top:* $b_{\text{sml,p}}dN_p/dz$ combined for all tracers, with best-fit spline plotted in blue and 100 splined samples drawn from diagonal Gaussian realizations of the noise overplotted in gray. The difference in dN/dz between the two halves of the sky (split at $\ell = 155^\circ$; not shown) is comparable to the range of the 100 spline realizations. *Middle:* dN/dz from the COSMOS cross-matches (thick solid lines) compared to dN/dz from 44 COSMOS-like $\sim 2\text{deg}^2$ patches of HSC (gray lines). While HSC is deep enough to contain nearly all of the WISE objects, its photometric redshifts become biased at $z > 1$ and therefore we do not display them in this range. *Bottom:* Spline fit to the COSMOS dN/dz (thick solid line) compared to 44 realizations of the noise assuming diagonal Gaussian errors (thin gray lines). To account for cosmic variance, the standard deviation is a fixed multiple of the Poisson error set to match the observed scatter from the 44 HSC patches at $z < 1$, as described in Section 5.1.

certainties. To create a smooth and physical dN_p/dz , we therefore model $b_{\text{sml,p}}dN_p/dz$ using cubic B-splines with the spline coefficients required to be positive, satisfying the positivity constraint on $b_{\text{sml,p}}dN_p/dz$. Considering the penalized χ^2 :

$$\chi^2 = \sum_i \left(\frac{\hat{y}_i - y_i}{\sigma_i} \right)^2 + \lambda \int dx [\hat{y}''(x)]^2 \quad (5.11)$$

we determine λ by minimizing χ^2 using cross-validation [99]. This method is sufficiently flexible to fit almost any shape of $b_{\text{sml,p}}dN_p/dz$, while satisfying our constraints. We use knots evenly spaced between $z = 0.1$ and $z = 3.5$ with $\Delta z = 0.2$.

By requiring \hat{y} to be positive, this procedure introduces a bias into the theory predictions for C_ℓ , since in regions of nearly zero dN/dz , we will fit to positive noise fluctuations but

not negative noise fluctuations. Moreover, the magnitude of this bias is different for $C_\ell^{\kappa g}$ and C_ℓ^{gg} . We find that the differential bias is generally small ($< 5\%$) and therefore do not consider it further in this paper. However, cosmological parameter constraints from these data will require a more careful approach [26], such as simulating the C_ℓ and dN/dz measurement given some known input cosmology and dN/dz , and subtracting the contribution to C_ℓ from the bias in dN/dz .

We create smooth dN/dz in a similar fashion for the cross-match redshifts. Here we use bins of $\Delta z = 0.06$ instead, as we find that more knots are required to accurately represent the shape of the cross-match dN/dz .

We propagate errors on dN/dz by drawing 100 samples from the data (assuming uncorrelated Gaussian errors between redshift bins), finding the best-fit dN/dz , and using it to model the auto and cross-power spectra. Additionally, we test the assumptions behind the jackknife dN/dz errors by splitting the sky in half at Galactic $\ell = 155^\circ$ and measuring dN/dz separately for each half. Summary statistics for both the cross-correlation and cross-match redshifts are given in Table 2.

5.3 Systematic errors in the cross-correlation dN/dz

One source of systematic error in the measurement of dN/dz is the discrepancy between $b_{\text{sml,p}}$, as measured by the configuration space photometric-spectroscopic cross-correlations, and $b_{\text{lin,p}}$, as required to model the autospectra and CMB cross-spectra. Exactly matching the scales used for the cross-correlation redshifts and the CMB cross-correlations is undesirable because it would push the cross-correlation redshifts to large scales where the signal-to-noise is lower and the potential impact of observational systematics is larger [61]; indeed, previous work uses scales of several Mpc at most [61, 64, 66–68, 72–74]. Conversely working on very small scales can be problematic, as the cross-correlation could depend upon galaxy formation physics in addition to the redshift distribution.

To study potential deviations between $b_{\text{sml,p}}$ and $b_{\text{lin,p}}$, we populate an N -body simulation with a simple HOD model for the WISE galaxies (Appendix B), which is roughly consistent with the spectroscopic cross-clustering given the cross-match dN/dz (Figure 19). We then measure b_{sml} and b_{lin} from the autocorrelation of halos in the simulation at four representative redshifts ($z = 0.41, 1.00, 1.27$ and 1.78 ; Figure 17). At $z = 0.41$, b_{sml} is 0.7% (1.7%, 2.5%) greater than b_{lin} for halos representative of the blue (green, red) samples. At $z = 1.78$, b_{sml} is 7.2% (15.3%) greater than b_{lin} for green (red) halos; and at $z = 1.00$, b_{sml} is 1.6% greater than b_{lin} for blue halos. We discuss the implications of these discrepancies between $b_{\text{sml,p}}$ and $b_{\text{lin,p}}$ in Section 7; we find that their impact is subdominant to the statistical uncertainty on dN/dz .

We also compare the fiducial real-space $b_{\text{sml,p}}dN_p/dz$ to $b_{\text{lin,p}}dN_p/dz$ measured in Fourier space using Eq. 5.1 on the same angular scales ($\ell = 100$ to 1000) as the CMB lensing cross-correlation.²² We find good agreement for bdN/dz in both configuration and harmonic space (Figure 8), suggesting that discrepancies between $b_{\text{sml,p}}dN_p/dz$ and $b_{\text{lin,p}}dN_p/dz$ are minor.

We test the sensitivity of the dN/dz results to the presence of angular systematics in the spectroscopic data by measuring the weighted cross-correlation, using the combined angular systematics, fiber collision and redshift failure weights for BOSS galaxies and eBOSS; and the inverse of the targeting completeness for BOSS quasars. We also create and apply

²²At $z < 0.3$, $\ell_{\text{max}} = 1000$ corresponds to $k_{\text{max}} > 1 h \text{ Mpc}^{-1}$, and the scale-independent bias assumption begins to break down. As a result, we set $\ell_{\text{max}} = \min(1000, k_{\text{max}}\chi)$, where χ is the comoving distance to the redshift bin center and $k_{\text{max}} = 2.5 h \text{ Mpc}^{-1}$.

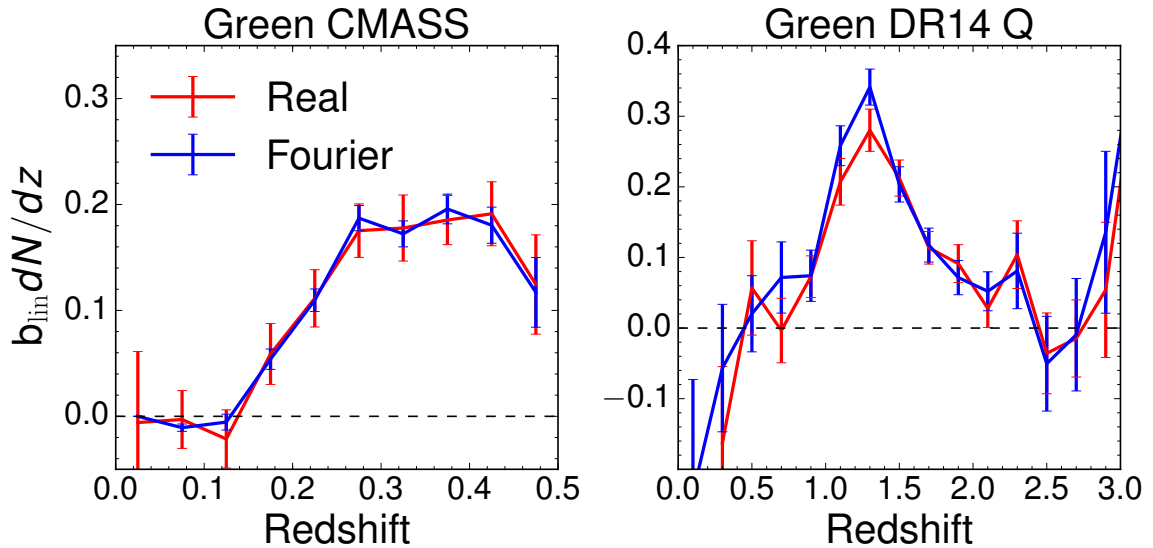


Figure 8. Comparison between the fiducial $b_{\text{sml,p}} dN_{\text{p}}/dz$ measured in configuration space (Equation 5.4) and $b_{\text{lin,p}} dN_{\text{p}}/dz$ measured in harmonic space using the pipeline described in Section 4, with $100 < \ell < 1000$.

systematics weights for the unWISE samples, following the methodology of ref. [85] for the BOSS and eBOSS samples. We construct $n_{\text{side}}=128$ maps of the unWISE density (correcting for sub-pixel masking) and of several systematics: stellar density from Gaia [42], 5σ limiting magnitude in W2, and N_{HI} column density from the HI4PI 21 cm survey [100]. We fit piecewise linear functions to the relationship between density and systematic, using stellar density and W2 limiting magnitude for the green and blue samples, and stellar density and N_{HI} for the red sample (other maps are not significantly correlated with galaxy density). We then define the weights for each systematic as the inverse of the predicted density.

We found $< 0.8\sigma$ change between the weighted and unweighted cross-correlations among all bins in redshift, spectroscopic and photometric tracers; this suggests that angular systematics correlated with unWISE fluctuations do not significantly affect our results.

We also compare the observed cross-correlation in a given redshift bin to the cross-correlation between Gaia stars and the spectroscopic sample. Since $\sim 2\%$ of all unWISE samples are stars, star-driven fluctuations in the spectroscopic sample may lead to spurious correlations between unWISE and spectroscopic samples. We find that the LOWZ-Gaia cross-correlation, times a fiducial stellar contamination fraction of 2%, is $< 5\%$ of the LOWZ-unWISE cross-correlation at $z > 0.15$, but comparable to the LOWZ-unWISE cross-correlation at $z < 0.15$ (for all three colors), although the error bars on the LOWZ-Gaia cross-correlation are comparable to the measured cross-correlation at these redshifts.

6 Galaxy-lensing auto and cross-spectra

In this section we present our measurements. We parameterize the amplitude of the correlations by a single effective linear bias

$$b^{\text{eff}} = \int dz b_{\text{lin,p}}(z) \frac{dN_{\text{p}}}{dz} \quad (6.1)$$

where we follow our convention of $\int dz dN/dz = 1$. For our theory model, we use the cross-correlation redshifts, $b_{\text{sml,p}} dN_p/dz$, to approximate b^{eff}

$$b^{\text{eff}} \approx \int dz b_{\text{sml,p}}(z) \frac{dN_p}{dz} \quad (6.2)$$

We insert the normalized cross-correlation redshifts, $f(z) dN_p/dz$

$$f(z) \frac{dN_p}{dz} \equiv \frac{b_{\text{sml,p}}(z) \frac{dN_p}{dz}}{b^{\text{eff}}} \quad (6.3)$$

into equation 3.2, and allow the amplitude b^{eff} to vary to match the data:

$$C_\ell^{\kappa g} = b^{\text{eff}} \int d\chi \frac{W^\kappa(\chi)}{\chi^2} H(z) \left[f(z) \frac{dN_p}{dz} \right] P(k\chi = \ell + 1/2) \\ + \int d\chi \frac{W^\kappa(\chi) W^\mu(\chi)}{\chi^2} P(k\chi = \ell + 1/2) \quad (6.4)$$

$$C_\ell^{gg} = (b^{\text{eff}})^2 \int d\chi \frac{1}{\chi^2} H(z)^2 \left[f(z) \frac{dN_p}{dz} \right]^2 P(k\chi = \ell + 1/2) \\ + b^{\text{eff}} \int d\chi \frac{W^\mu(\chi)}{\chi^2} H(z) \left[f(z) \frac{dN_p}{dz} \right] P(k\chi = \ell + 1/2) \\ + \int d\chi \frac{W^\mu(\chi) W^\mu(\chi)}{\chi^2} P(k\chi = \ell + 1/2) \quad (6.5)$$

For the magnification bias term $W^\mu(\chi)$, we take the cross-matched dN/dz , and the values of s from Appendix C.

Figure 9 shows the auto correlation of our three galaxy samples as well as their cross-correlation with the CMB lensing convergence, κ . Table 4 summarizes the results. We quote both statistical and dN/dz error bars on b^{eff} ; the statistical errors are from the errors on C_ℓ^{gg} and $C_\ell^{\kappa g}$ using the fiducial dN/dz , whereas the dN/dz error bars are the standard deviation of b^{eff} from fitting C_ℓ^{gg} and $C_\ell^{\kappa g}$ to 100 samples of dN/dz with uncorrelated Gaussian error added (as described earlier).

Over the range of scales that we model ($100 < \ell < 1000$), we obtain cross-correlation $S/N = \sqrt{\chi_{\text{null}}^2 - \chi_{\text{cross}}^2}$ of 59.2, 68.5 and 41.4 for the blue, green and red samples, respectively. The combined cross-correlation S/N for the sample as a whole (taking into account the covariance between the three galaxy samples) is 79.3.

7 Systematics in the cross-correlation and null tests

In this section we explore the impact of stellar contamination, foregrounds in the CMB maps and the galactic latitude dependence of the signal.

7.1 Stellar Contamination

Due to the photometric nature of the catalog, with only two broad-band filters available, some fraction of the objects in our catalog will be stars or other non-cosmological sources

WISE sample	$b_{\text{auto}}^{\text{eff}}$	Shot Noise ($\times 10^7$)	σ_b from dN/dz	$\chi^2_{\text{auto}}/\text{dof}$	$b_{\text{cross}}^{\text{eff}}$	σ_b from dN/dz	$\chi^2_{\text{cross}}/\text{dof}$
Blue	1.74 ± 0.0052	0.92 ± 0.012	0.0865	24.3/4	1.56 ± 0.0276	0.0355	6.11/5
Green	2.44 ± 0.0083	1.81 ± 0.012	0.0793	8.69/4	2.23 ± 0.0352	0.0308	2.93/5
Red	3.47 ± 0.0383	29.6 ± 0.09	0.2435	8.21/4	3.29 ± 0.090	0.1541	4.56/5

Table 4. Results from fitting a constant bias times HaloFit power spectrum (using cross-correlation dN/dz). Note that the value of χ^2 here is for a *fixed* fiducial dN/dz and for a linear bias model with HaloFit power spectrum. A high χ^2 value indicates the need to marginalize over the redshift distribution for any cosmological interpretation, and highlights the importance of going beyond linear bias. In the follow up paper [26], we fully marginalize over the uncertainty in dN/dz and a non-linear model for galaxy biasing, obtaining a good fit.

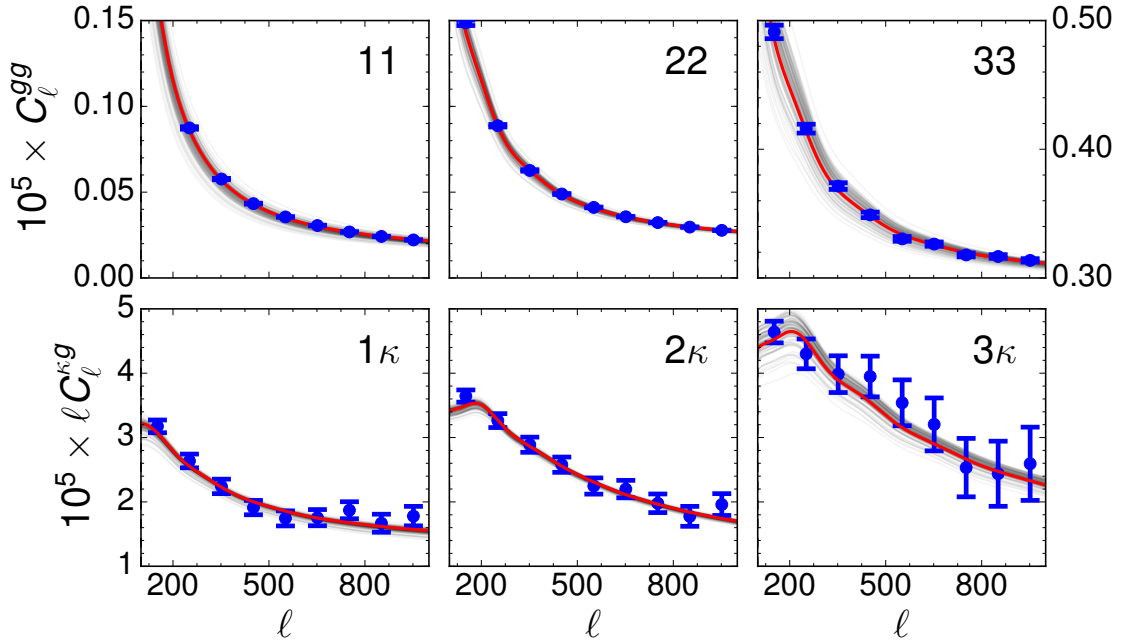


Figure 9. Auto correlation (top) and cross correlation between the unWISE catalog and Planck CMB lensing (bottom); numbers label the samples (1: blue, 2: green, 3: red). The best-fit theory curve assuming a constant bias times HaloFit is shown as a solid red line and the uncertainty in the model from the uncertainty in dN/dz is given by the gray lines. We fit angular scales to the right of the dashed line. Magnification bias is a few times larger than the errorbars in the auto-spectra, and $\sim 50\%$ of the errorbars in the CMB cross-spectra.

such as nebulae or artifacts in the images. For simplicity, below we shall refer to any non-cosmological source that is uncorrelated with the true galaxies in our samples as “stars.” On scales where stars can be considered unclustered, i.e. where their clustering power is negligible compared to the galaxies, their effect is to lower both the auto and cross correlations in a way that is completely degenerate with the galaxy bias, and hence can be marginalized over in a cosmological analysis. To see this, let’s assume that average number density of objects in our catalog, \bar{n} , is the sum of galaxies, \bar{n}_g , and “stars”, \bar{n}_s . The observed “galaxy overdensity”

necessarily includes both

$$g^{\text{obs}} = \frac{\delta n_g}{\bar{n}_g + \bar{n}_s} + \frac{\delta n_s}{\bar{n}_g + \bar{n}_s} \quad (7.1)$$

We expect the second term to be uncorrelated with CMB lensing, given its non-cosmological origin. This is an important assumption that can be violated, for example, if galactic dust emission affects CMB lensing reconstruction, and at the same time modulates the number density of galaxies observed in WISE. We test this in the next section by applying different galactic cuts. Assuming the second term is uncorrelated with κ , we can write

$$\langle \kappa g^{\text{obs}} \rangle = \langle \kappa g^{\text{true}} \rangle \frac{\bar{n}_g}{\bar{n}_g + \bar{n}_s} = \langle \kappa g^{\text{true}} \rangle \frac{1}{1 + \epsilon_s} \quad (7.2)$$

where we have defined $\epsilon_s = \bar{n}_s/\bar{n}_g$ to be the stellar contamination fraction. Similarly, on scales where stars are approximately unclustered (see below),

$$\langle g^{\text{obs}} g^{\text{obs}} \rangle = \langle g^{\text{true}} g^{\text{true}} \rangle \left(\frac{1}{1 + \epsilon_s} \right)^2 \quad (7.3)$$

From the argument above, we can see that the effect of stellar contamination is to lower the auto and cross correlations in a scale-independent way. Since $\langle \kappa g^{\text{true}} \rangle \propto b_g$ and $\langle g^{\text{true}} g^{\text{true}} \rangle \propto b_g^2$, we conclude that unclustered stellar contamination is completely degenerate with a scale-independent galaxy bias and that our analysis actually measures the “effective bias”

$$b^{\text{eff}} = b^{\text{true}} \frac{1}{1 + \epsilon_s} \quad (7.4)$$

so that marginalization over galaxy bias will automatically also marginalize over the (in general unknown) amount of stellar contamination. We further note that the ratio

$$\frac{(C_\ell^{\kappa g})^2}{C_\ell^{gg}} \sim \frac{(b_g^{\text{eff}})^2 \sigma_8^4}{(b_g^{\text{eff}})^2 \sigma_8^2} \sim \sigma_8^2 \quad (7.5)$$

is proportional to σ_8^2 in linear theory, and is therefore independent of b^{eff} on linear scales.

The power spectrum of galactic contaminants such as stars is typically very large on large scales, falling off steeply with increasing ℓ (faster than the typical galaxy power spectrum). For example, we have checked that if the stellar contamination in unWISE traces a Gaia stellar map²³ with stellar contamination fraction $\sim 1\%$ (as expected from the cross-match to COSMOS), the stellar power in the lowest- ℓ bin used in the analysis is $< 0.5\%$ of the galaxy clustering power on the same scale, ensuring that the argument above holds.

7.2 Foreground contamination to CMB lensing cross-correlations

The Minimum Variance (MV) reconstruction we use in the fiducial analysis is dominated by CMB temperature (rather than polarization), and is therefore subject to possible contamination by both galactic and extragalactic foregrounds. When these foregrounds are correlated with the galaxy sample of interest, they can lead to biases in the cross-correlation [30–33, 101].

Regarding galactic foregrounds, we expect the largest contaminant to be galactic dust, seen in emission in the CMB maps, and causing reddening and/or extinction on most galaxy catalogs. Imperfect foreground separation can impact the CMB lensing maps. While we

²³We also find a similar power spectrum for Gaia stars that meet our blue or green WISE color selection.

expect the IR-selected unWISE sources not to be directly affected by galactic dust, nonetheless their local density can be dependent on (for example) stellar density, which is itself correlated with galactic dust. The Planck team [25] performed a large number of null tests regarding the reconstructed map, and find general stability of the baseline reconstruction on the SMICA component separated temperature map. Importantly, the reconstruction is stable with respect to choice of galactic mask, with variations consistent with those expected from the change in area. Most of the null test tensions come from the reconstruction on the 217 GHz frequency map, which may contain non-negligible galactic contamination. We caution that the tSZ-free map has larger weight given to the 217 GHz channel and may therefore have a larger dust contamination.

Regarding extragalactic foregrounds, the effect on the lensing auto-power spectrum has been thoroughly investigated in Section 4.5 of ref. [25]. The Planck team has found that at lensing $\ell < 1000$, both tSZ and CIB biases are expected to be a small fraction of 1%, significantly below the statistical errors. The effect of kSZ biases for the Planck SMICA map has been calculated in ref. [101] and shown to be negligible. Calculating the bias to the cross-correlation with galaxies is more difficult, since it depends on the particular sample, its redshift distribution, HOD and IR luminosity function. Using realistic correlated CMB and large-scale structure simulations, refs. [30, 101] have found that for a galaxy sample with median redshift ≈ 0.8 and $b(z) \approx 1 + 0.84z$, the size of the biases in auto and cross-correlations are very comparable. This sample is rather similar in redshift distribution and bias (and hence mass) to the WISE blue and green samples, and therefore we expect that the biases in cross be the same order of magnitude of the ones in the CMB lensing auto-spectrum, and hence safely sub-percent. While this argument only provides a rough estimate, it appears very likely that any extragalactic source of bias will be well below the statistical significance of our cross-correlations.

As a further test, we repeat the cross-correlation with the Planck 2018 lensing reconstructed from tSZ-deprojected temperature maps, shown in Table 5. Apart from removing the possible tSZ contamination, the CIB contribution will be significantly different due to the different weighting of the single-frequency channels. While the absence of tSZ bias could in principle be partly compensated by a larger CIB-induced bias, the consistency between the fiducial and tSZ-free cross-correlations provides further confidence that foreground contamination is subdominant to our other sources of uncertainty.

WISE sample	$b_{\text{cross}}^{\text{eff}}$	$\chi_{\text{cross}}^2/\text{dof}$	$b_{\text{cross,tSZ-free}}^{\text{eff}}$	$\chi_{\text{cross,tSZ-free}}^2/\text{dof}$
Blue	1.56 ± 0.0276	6.11/5	1.54 ± 0.0305	9.34/5
Green	2.23 ± 0.0352	2.93/5	2.19 ± 0.0389	3.87/5
Red 16.2	3.29 ± 0.090	4.56/5	3.25 ± 0.102	6.03/5

Table 5. Comparison between fiducial $b_{\text{cross}}^{\text{eff}}$ (reproducing Table 4) and $b_{\text{cross}}^{\text{eff}}$ for the tSZ free sample.

7.3 Galactic mask dependence of the sample properties

If the redshift distribution varies across the sky, the clustering dN/dz measured in the SDSS region could be unrepresentative of the true dN/dz across the entire WISE mask. We test this possibility by restricting the C_{ℓ}^{gg} and $C_{\ell}^{\kappa g}$ measurement to the SDSS footprint used to measure dN/dz and repeating our measurements. We find good agreement between the biases measured in the SDSS region and the biases measured across the full sky (Table 6). We also

find that the galaxy-galaxy cross-spectra (i.e. Fig. 22) are quite similar in the SDSS region as in the full unWISE footprint, changing by $< 10\%$.

WISE sample	$b_{\text{auto}}^{\text{eff}}$	$10^7 \times \text{Shot Noise}$	$\chi_{\text{auto}}^2/\text{dof}$	$b_{\text{cross}}^{\text{eff}}$	$\chi_{\text{cross}}^2/\text{dof}$
Blue	1.76 ± 0.0117	0.87 ± 0.027	10.3/4	1.55 ± 0.0632	12.7/5
Green	2.42 ± 0.0188	1.78 ± 0.027	10.1/4	2.19 ± 0.0797	11.8/5
Red 16.2	3.60 ± 0.0845	28.9 ± 0.21	7.27/4	3.27 ± 0.206	5.73/5

Table 6. Results from fitting a constant bias times HaloFit power spectrum (using cross-correlation dN/dz), restricting measurements to the CMASS area.

We further test the impact of restricting our sample to higher Galactic latitudes by sequentially applying the Planck 60%, 40% and 20% Galactic masks (retaining the “cleanest” 60, 40 and 20% of the extragalactic sky)²⁴ in addition to the standard WISE masks described in Section 2.4. We find no significant change in C_{ℓ}^{rg} as the Galactic masking is changed. In contrast, we find changes of several percent with differing Galactic masks in the $\ell < 100$ bin; consequently, we only fit the bias to $\ell > 100$. At $\ell > 100$, we find a mild scale-independent trend in the amplitude of C_{ℓ}^{gg} with Galactic latitude, which may be caused by changes in the galaxy population due to changing selection function at higher Galactic latitudes (modifying both the bias and dN/dz). This should not affect our cosmological constraints as long as the area over which we measure dN/dz and the auto and cross correlations are the same. In practice, we prefer not to restrict the dN/dz measurement to the footprint of the spectroscopic samples ($f_{\text{sky}} = 0.15$) and find that measuring b^{eff} over the spectroscopic footprint leads to variations $< 1\sigma$, suggesting dN/dz varying on the sky is not a major systematic.

Changes in the galaxy-galaxy cross-spectra with Galactic latitude suggest that dN/dz does vary on the sky in addition to the bias. If only the bias were changing as we changed the Galactic masks, the increase in the cross-spectrum would go as the geometric mean of the increase in the individual galaxy auto-spectra, but the red-blue and red-green cross-correlations increase by $\sim 5-10\%$ more than the geometric mean, implying a varying dN/dz ²⁵ or more complex bias.

We perform a similar test for masking the ecliptic plane below $\beta = 30^\circ, 45^\circ, 60^\circ$ and 80° (Figure 11). Similarly, we find only mildly scale-dependent trends, with deviations of $\sim 5\%$ in the auto-spectrum at $\ell > 100$.

We also find that doubling the WISE stellar masking radius changes b^{eff} by less than 1σ . Similarly, applying the more conservative masks of ref. [102] (both the QSO and ELG masks, equation 20, which mask around considerably fainter stars than our mask) changes b^{eff} by less than 0.5σ .

7.4 Systematic uncertainties in the redshift distribution

Due to the $6''$ WISE PSF, blending is a source of systematic error in the cross-match redshifts, as it could lead to spurious matches with COSMOS. Many of our sources are blended, and it is possible that the low-redshift tails in the red and green samples result from source blending rather than from the presence of low-redshift sources. However, because we only use the

²⁴Available at https://irsa.ipac.caltech.edu/data/Planck/release_2/ancillary-data/masks/HFI_Mask_GalPlane-apo0_2048_R2.00.fits

²⁵Using fainter red samples (e.g. with a faint cut at $W2 = 16.5$ or 16.7) leads to even larger variation in red cross blue compared to red and blue separately, suggesting that dN/dz variations are more severe for the fainter red samples.

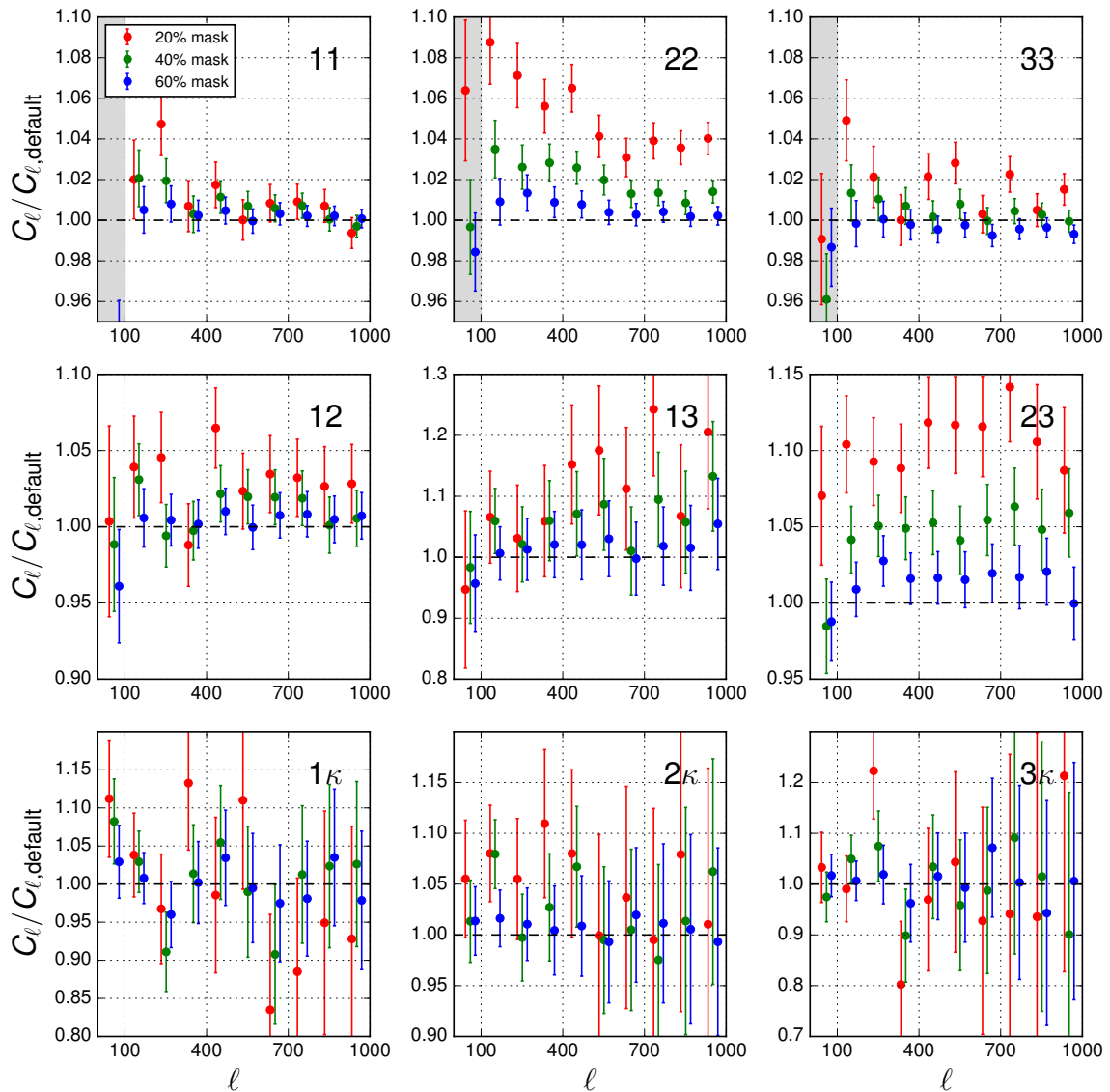


Figure 10. Change in clustering when masking is changed from the default Planck and WISE masks to the Planck 20%, 40% and 60% Galactic masks. Top row shows galaxy auto-spectra, middle row shows galaxy-galaxy cross-spectra, and bottom row gives galaxy-CMB cross spectra. Gray regions indicate scales excluded ($\ell < 100$) because the power depends too strongly on the Galactic mask.

cross-match redshifts in the magnification bias term, we expect blending to have a negligible impact on $b_{\text{auto}}^{\text{eff}}$ and $b_{\text{cross}}^{\text{eff}}$. If we replace all unWISE magnitudes in the cross-match with Spitzer 3.6 and 4.5 μm magnitudes (reducing the possibility of source confusion due to the 2'' resolution of Spitzer) and replace the cross-match dN/dz with the Spitzer dN/dz , we find shifts of $< 0.5\sigma$ in the fitted biases.

Systematic errors in the COSMOS dN/dz may also impact our results, and are an important systematic in cosmic shear [103, 104]. Again, because we only use the COSMOS dN/dz in the magnification term, the impact of this systematic shift on our results is limited. Because our redshift bins are broad, the impact of scatter in the photometric redshifts should

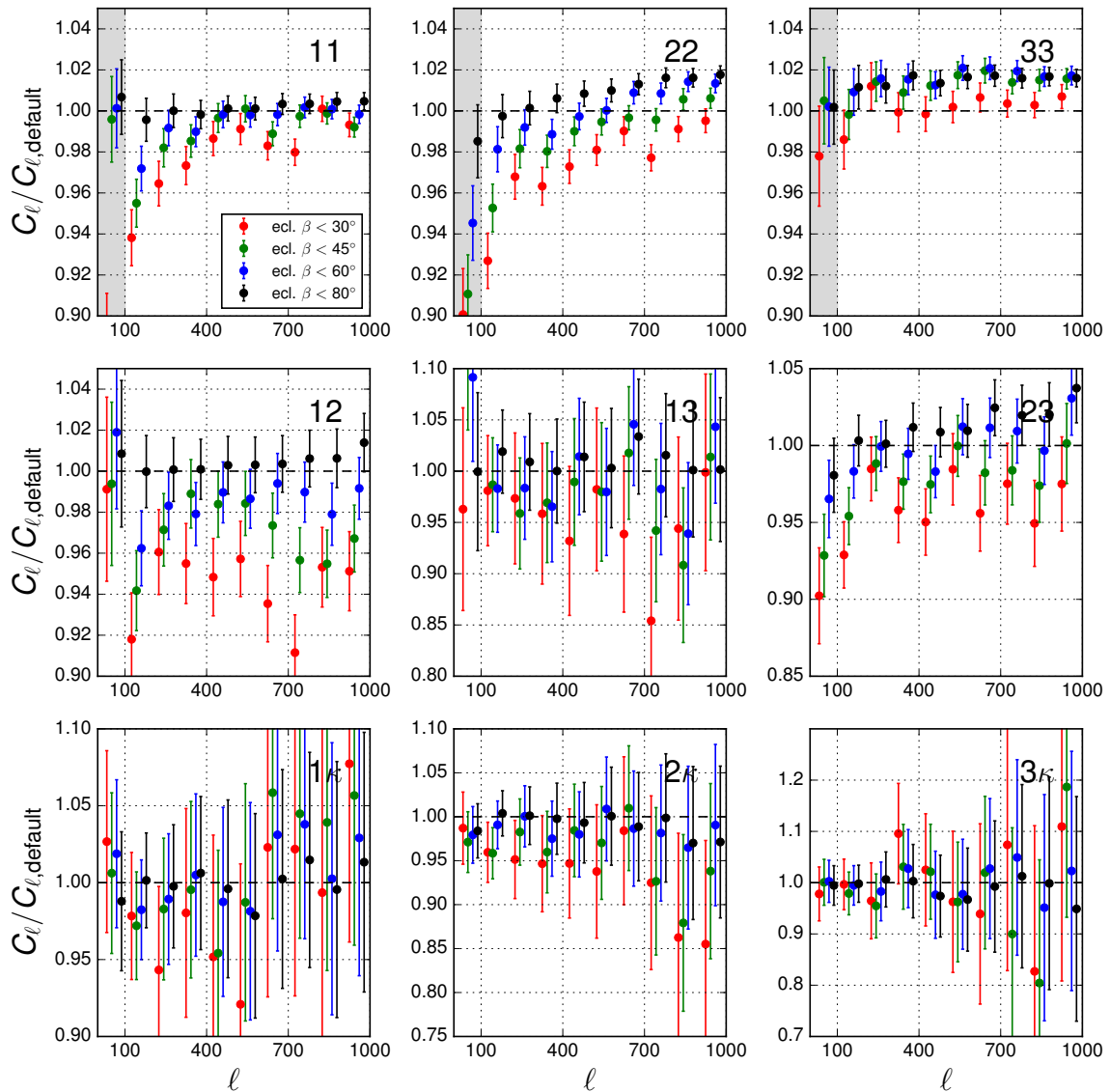


Figure 11. Change in clustering when masking is changed from the default Planck and WISE masks to cover more of the ecliptic. We sequentially exclude the sky at ecliptic latitude $\beta < 30^\circ$, 40° , 60° , and 80° (i.e. black points include the smallest fraction of the sky, near the Ecliptic poles). Since the WISE depth of coverage is highest at the ecliptic poles, the black points are the deepest and the red points are the shallowest. Top row shows galaxy auto-spectra, middle row shows galaxy-galaxy cross-spectra, and bottom row gives galaxy-CMB cross spectra. Gray regions indicate scales excluded ($\ell < 100$) because the power depends too strongly on the Galactic mask.

be minimal, as the scatter is $\Delta z < 0.1$ for the three samples, compared to the $\Delta z \sim 0.5$ redshift bins. Catastrophic errors may have a more significant impact; from Figures 11 and 12 in ref. [41], we conservatively estimate 10% catastrophic errors for the higher-redshift $i \lesssim 24$ red and green samples, and 1% catastrophic errors for the $i \lesssim 22$ blue samples. The maximum impact of these errors would be to create a population of galaxies with $\Delta z \sim 1$ redshift errors. We therefore create two dN/dz for the green and red samples where 10% of

the galaxies are scattered uniformly into a $0 < z < 1$ tail or a $2 < z < 3$ tail. We find that using these dN/dz instead of the fiducial dN/dz makes $\lesssim 0.5\sigma$ difference in our results.

We study the impact of a discrepancy between $b_{\text{sml,p}}$ and $b_{\text{lin,p}}$ using b_{sml} and b_{lin} from the autocorrelation of WISE-like samples in an N -body simulation (Appendix B). We parameterize $b_{\text{sml}}/b_{\text{lin}} = 1 + Az^2$ (smooth curves in Figure 18), allowing A to vary between zero and twice its fiducial value, A_{fid} . We pick $1 + Az^2$ because it has roughly the right functional form. Since the HODs are approximate anyway, quantitative agreement with the N -body results is not required. Indeed, the $1 + Az^2$ fitting function is somewhat conservative, as it predicts a slightly larger increase in $b_{\text{sml}}/b_{\text{lin}}$ than indicated by the N -body simulations (compare the N -body simulations to the fitting function at $z \sim 0.4$). We show the impact of using both the fiducial value, $A_{\text{fid}} = 0.025, 0.025, 0.05$ for blue, green and red, and the maximal value, $A_{\text{max}} = 0.1, 0.15, 0.2$ for blue, green and red, for the most extreme bias evolution allowed by the data.

We summarize the impact of different systematics on $b_{\text{auto}}^{\text{eff}}$ and $b_{\text{cross}}^{\text{eff}}$ for the green sample in Figure 12. The analogous plots for the blue and red samples look similar; in fact, green is the only sample to have $> 1\sigma$ discrepancies from the fiducial value (measured using the quadrature sum of the dN/dz error and the statistical error), with a 1.3σ discrepancy when using A_{max} to correct for nonlinear bias evolution and a 1.3σ discrepancy when the cross-match dN/dz uses $r_{\text{p,min}} = 4 h^{-1}$ Mpc (where $r_{\text{p,min}}$ indicates the minimum separation bin used in the clustering redshifts, fiducially $2.5 h^{-1}$ Mpc). For the $r_{\text{p,min}} = 4 h^{-1}$ Mpc dN/dz , we use the error for the $r_{\text{p,min}} = 4 h^{-1}$ Mpc dN/dz for σ rather than the quadrature sum of this error and the error from the fiducial $r_{\text{p,min}} = 2.5 h^{-1}$ Mpc dN/dz , because the two dN/dz errors are highly correlated.

8 Conclusions and lessons learned

We have presented a tomographic measurement of the cross-correlation of the unWISE galaxies and CMB lensing. We report a combined detection significance of 55.1, which is the highest-significance detection of lensing by large-scale structure to date.

One of the greatest challenges was the characterization of the redshift distribution for the three samples. Since for most galaxies only the W1 and W2 magnitudes were available, we did not attempt to assign individual photometric redshifts, but just split the full catalog into three samples with different mean redshifts, but with non-negligible overlap between them. We use two techniques to measure the redshift distribution.

First, we cross-match our objects with the COSMOS catalog, obtaining a direct measurement of the redshift distribution dN/dz . A direct cross-match is insensitive to modeling assumptions and measures dN/dz , required to calculate the magnification bias contribution. If used to predict clustering, assumptions on the redshift evolution of the bias evolution are necessary. One disadvantage is the high completeness required of the survey, which limits the area available. Another disadvantage is source blending, which could lead to spurious cross-matches and thus modify dN/dz . The small overlap area (2 square degrees) not only limits the measurement statistically, but given the inhomogeneous depth of the WISE survey and possible spatial dependence of the selection function, the results may not be representative of the full WISE footprint. While we take steps to ensure that our catalogs are magnitude limited over the whole footprint by applying appropriate magnitude cuts, residual effects such as blending and background subtraction can potentially lead to inhomogeneity in the selection

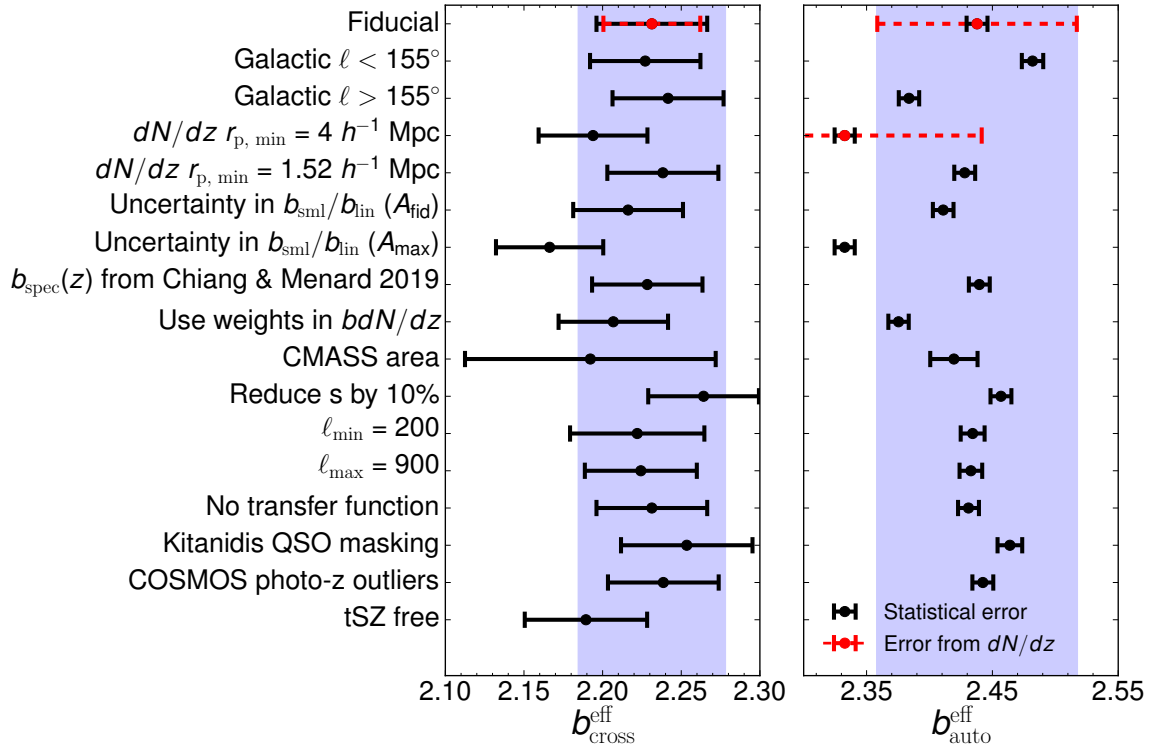


Figure 12. Impact of systematic errors on b^{eff} for the green sample. Black errorbars give the statistical uncertainty, red dashed errorbars give the systematic uncertainty from errors in dN/dz (only plotted for the fiducial values), and the blue band displays their quadrature sum. We also plot the uncertainty from dN/dz error for the $r_{p, \text{min}} = 4 h^{-1} \text{ Mpc}$ dN/dz , to emphasize that this point is only 1.3σ discrepant if we define σ using the dN/dz errors. Top row gives fiducial value matching Table 4. The next two rows show b^{eff} for the split-sky sample, giving an estimate of uncertainty due to uncertain dN/dz . The next four rows are concerned with nonlinear bias evolution; either by increasing/decreasing $r_{p, \text{min}}$ to be more/less robust against nonlinear bias; or using the parameterized function from Appendix B, $b_{\text{sml}, p}/b_{\text{lin}, p} = (1 + Az^2)$ with A_{fid} (A_{max}) = 0.025 (0.1), 0.025, (0.15), 0.05 (0.2) for blue, green and red. The next row shows the impact of changing the CMASS and LOWZ spectroscopic bias evolution used in the clustering redshifts from the measured values of Table 7 to values from Fig. 12 of Ref. [98]. The next rows show the impact of using weights in the cross-correlation redshifts, restricting to the CMASS footprint (Table 6), reducing magnification bias response s by 10%, changing scale cuts for the auto- and CMB-cross power spectra, using the tSZ-free lensing map, using stricter stellar masking from ref. [102], and the impact of COSMOS photo- z catastrophic errors adding a spurious low- z tail to dN/dz .

function. The mild trends in bias with respect to Galactic mask observed in Figure 10 may be an indication of this.

Second, we cross-correlate the unWISE samples with a number of overlapping spectroscopic samples, thus determining the product of the bias and redshift distribution. This can be advantageous when calculating the clustering signal, since it is this product that enters the auto-correlation and the cross-correlation with CMB lensing. Another advantage is the typically large overlap area (important for when the selection function is inhomogeneous), and the fact that there are no completeness requirements on the spectroscopic sample. However, assumptions on the redshift evolution of the bias are necessary when calculating the magni-

fication bias contribution, and the impact of magnification needs to be taken into account in the spectroscopic-photometric cross-correlation. Moreover, this measurement is subject to the usual modeling challenges such as non-linearities in clustering and bias.

As discussed in Appendix B, the two measurements of dN/dz are consistent with each other when assuming a simple model for bias evolution. Further, the consistency of the unWISE bias measured on the CMASS overlap region (Table 6) compared to the whole unWISE footprint (Table 4) indicates that the cross-correlation redshifts should be unaffected by spatial variations in the selection function. In the fiducial analysis, we use the cross-correlation result to predict the clustering and the cross-matched distribution to predict magnification bias and therefore we don't need to assume a redshift evolution of the bias.

Once the redshift distribution is known (or the uncertainties appropriately marginalized over), theoretical modeling of the signal on intermediate to small scales is the next challenge. Non-linear corrections to both clustering and bias become important at ℓ of few hundred, where the statistical S/N is still large in each bandpower. This implies that even if dN/dz were known perfectly, our ability to extract cosmological information could still be limited by our theoretical models. We defer consideration of modeling the signal to future work [26].

In conclusion, we believe that the cross-correlations presented here are an extremely sensitive probe of late-time cosmology. A spectroscopic followup of a subsample of the sources as well as improved modeling of intermediate and small scales can lead to sub-percent measurement, with important possible applications for tests of gravity, measurement of neutrino masses and the properties of Dark Energy.

Acknowledgments

We thank David Alonso, Enea Di Dio, Yu Feng, Julien Guy, Colin Hill, Ellie Kitanidis, Alexie Leauthaud, Thibaut Louis, Emmanuel Schaan, David Schlegel, Uros Seljak, Blake Sherwin, Zachary Slepian, David Spergel, Katherine Suess and Michael Wilson for very useful discussions. S.F. is supported by the Physics Division at Lawrence Berkeley National Laboratory. M.W. is supported by the U.S. Department of Energy and by NSF grant number 1713791. This research used resources of the National Energy Research Scientific Computing Center (NERSC), a U.S. Department of Energy Office of Science User Facility operated under Contract No. DE-AC02-05CH11231. This work made extensive use of the NASA Astrophysics Data System and of the `astro-ph` preprint archive at `arXiv.org`.

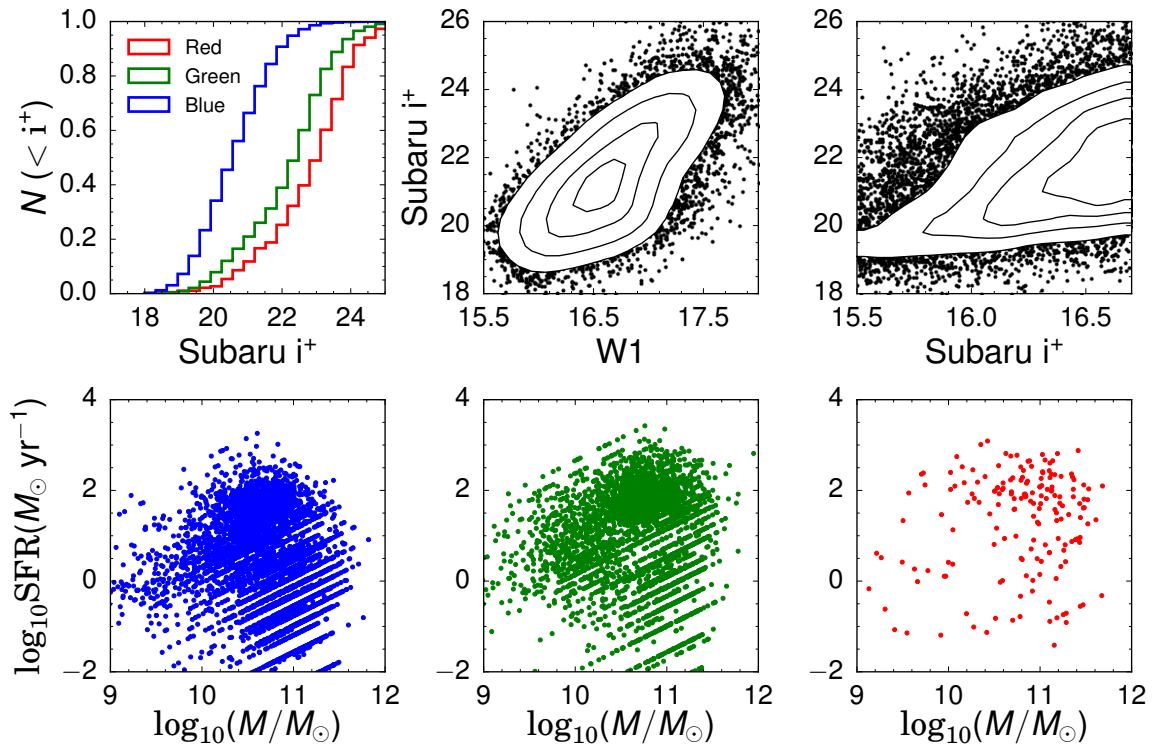


Figure 13. *Top left:* Distribution of Subaru i^+ magnitudes (“mag_auto,” measured in flexible elliptical apertures, as in ref. [105]) from unWISE matched to COSMOS. *Top center and right:* Subaru i^+ versus WISE W1 and W2 magnitudes for the combined red, green and blue samples in COSMOS. We show 20%, 40%, 60% and 80% iso-contours of the cumulative distribution function (Gaussian smoothed with $\sigma = 1$ mag) of galaxies in i^+ and W1/W2. *Bottom:* Distribution of stellar mass and star formation rate for each of the three samples, from COSMOS broad-band photometry.

A Optical properties of unWISE samples and prospects for spectroscopic followup

In this section, we describe the optical properties of the unWISE galaxies from archival photometric and spectroscopic data. We also discuss the prospects and requirements for spectroscopic followup of the unWISE samples to better determine dN/dz .

While the full unWISE sample only has infrared fluxes, by cross-matching to COSMOS we can determine the optical colors and properties of unWISE. In Figure 13, we show the distribution of Subaru i^+ for the unWISE galaxies, and the relationship between i^+ and the WISE bands. For the blue sample a 90% completeness is achieved at $i^+ \simeq 22$ while for the green and red samples 90% completeness occurs at $i^+ \simeq 24$.

We also show the stellar mass and star formation rates of unWISE galaxies from COSMOS broad-band photometry. All three unWISE samples have similar stellar masses (with $\log_{10}(M/M_{\odot}) = 10.80, 10.78,$ and 10.87 for the blue, green and red samples) but the star-formation rates of the green and red samples ($\log_{10} \text{SFR}/M_{\odot} \text{ yr}^{-1} = 1.03, 1.61$) are significantly higher than the star-formation rate of the blue sample ($\log_{10} \text{SFR}/M_{\odot} \text{ yr}^{-1} = 0.12$).

Some of the galaxies in the unWISE samples have been observed in the VVDS survey [106] using VIMOS on VLT, allowing us to both better characterize the galaxy samples and

understand the feasibility of spectroscopic followup. The VVDS-Deep survey has a simple selection function, uniformly targeting galaxies at $17.5 < I < 24$. Not every $17.5 < I < 24$ galaxy is targeted; to determine the completeness of the unWISE galaxies in VVDS, we must divide the number of matches by the VVDS targeting selection rate (typically 20-30%) and then compare to the number of unWISE galaxies lying within the VVDS spectroscopic mask.²⁶ We find 444, 261 and 13 VVDS matches to the blue, green and red samples (418, 191 and 10 with high confidence redshifts, ZFLAGS ≥ 2), implying 101.3%,²⁷ 89.6% and 70.0% of the blue, green and red samples yield a VVDS spectrum. This agrees well with the fraction of galaxies with $I < 24$, which is 99.6% (91.8%, 84.5%) for the three samples, implying that within the range of galaxies that could have been targeted, 97.8%, 69.0% and 59.4% of blue, green and red galaxies received a high-confidence VVDS redshift. VVDS-Deep exposure times are 4.5 hr on a $R \sim 230$ spectrograph, suggesting that spectroscopic followup of the unWISE samples is feasible on 8-10 m class telescopes (and perhaps smaller telescopes for the brighter blue sample).

We also incorporate galaxies from the VVDS UltraDeep survey, which includes 12, 19, and 1 galaxies from the blue, green and red samples (10, 11, and 1 with ZFLAGS ≥ 2). The redshift distribution of blue galaxies with redshifts from VVDS is quite similar to the COSMOS dN/dz (Figure 14); for the green sample, the VVDS dN/dz is suppressed relative to COSMOS at $z > 1.6$, possibly because of increased redshift failures at high redshifts where the [OII] line redshifts beyond the red end of the spectrograph.

We display three spectra from each sample in Figure 15, representing each sample at low, medium and high redshift. Blending presents a similar challenge for the VVDS cross-match as for COSMOS, so we only display galaxies that are well-isolated in optical imaging. Due to the paucity of red spectra, the red sources at $z = 0.477$ and $z = 2.27$ are blends, although in both cases only one of the two potential optical matches has a VVDS spectrum.

In Figure 16, we plot the distribution of redshift and rest frame [OII] 3727 Å EW for the green and blue samples from VVDS spectra, as well as $D_n(4000)$ versus [OII] 3727 Å EW, to separate star-forming from quiescent galaxies as in ref. [108]. We find median rest frame [OII] 3727 Å EW of 6.4 (11.8) Å in emission for the blue (green) sample, and from the star-forming versus quiescent cut from ref. [108], 29.0% (60.3%) of blue (green) galaxies are star-forming.

A direct measurement of dN/dz with smaller errors than the COSMOS cross-match dN/dz would allow for improved modeling of the unWISE samples and better control of systematic errors. Even with improved cross-match dN/dz , we would still require the photometric-spectroscopic cross-correlations to determine $b_{\text{lin}}(z)$, but we could greatly improve the simple HOD modeling in Appendix B and Fig. 19, allowing for better understanding of $b_{\text{lin}}(z)$ and potentially better control of systematics such as nonlinear bias evolution. With observations in several fields, we could also better understand the variation in dN/dz on the sky. Finally, we could better understand the impact of blending in our sample by re-targeting both (or all) galaxies blended together by the 6" WISE PSF.

If the errors on dN/dz were much smaller than the errors on the photometric-spectroscopic clustering measurement, we could neglect dN/dz errors and better model the unWISE galaxy population. This is not the case in Fig. 19; at $z < 0.2$ and $z \sim 0.5$ in the blue sample, the error

²⁶As with the COSMOS matches, we additionally remove VVDS galaxies with Spitzer-SWIRE [107] 4.5 μm magnitude > 19.2 (18.7 for red sample), although relatively few VVDS galaxies have SWIRE matches so this cut makes little difference.

²⁷Completeness higher than 100% likely indicates that the targeting selection rate is somewhat underestimated.

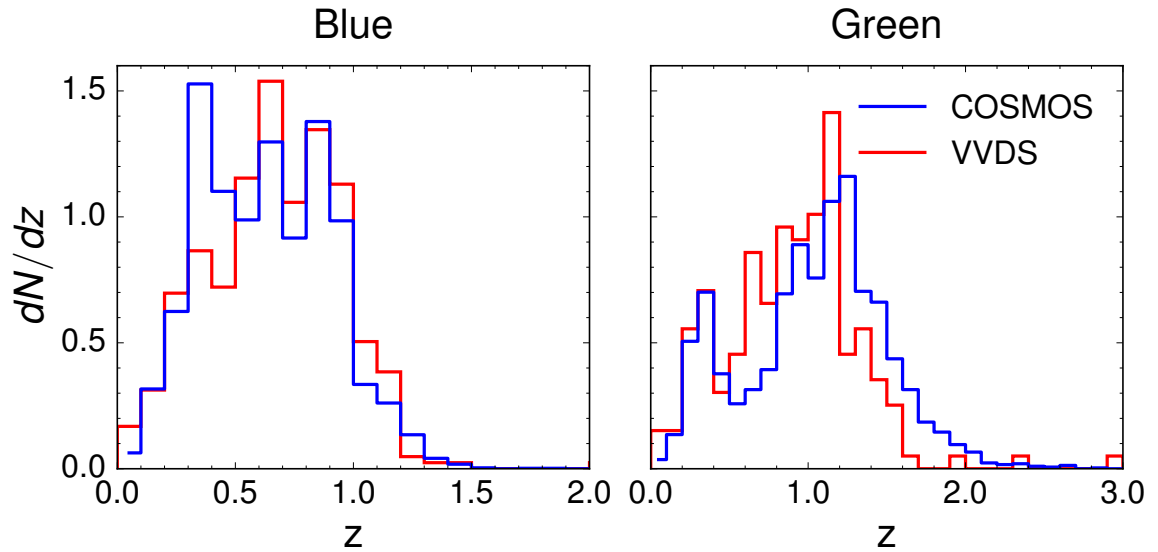


Figure 14. Comparison of dN/dz for COSMOS photometric (blue) and VVDS spectroscopic (red) matches for the blue and green samples (including spectra from VVDS-Deep and VVDS-UltraDeep). The red sample has too few VVDS matches to compare the two dN/dz . While VVDS is largely complete for the blue sample, incompleteness at the faint, high redshift end of the green sample may bias dN/dz relative to COSMOS.

from uncertain dN/dz (gray band) is larger than the statistical error on the clustering (blue errorbars). However, this is driven by the HSC-derived cosmic variance correction, which is a factor of 3.8 for the blue sample (Section 5.1). If instead of measuring dN/dz on a single field, we measured dN/dz in multiple fields spread across the sky, the errors would be dominated by Poisson rather than cosmic variance, and no such correction would be necessary. Indeed, if we divide out this correction in the dN/dz errors in Figure 19, we find that dN/dz errors are at most 80% of the statistical errors for blue and green (peaking at $z \sim 0.3 - 0.5$); for red, the dN/dz errors are larger at low redshift, 150% of the statistical errors at $z \sim 0.5$. Scaling from the number of galaxies with secure COSMOS redshifts (5557, 3024, and 164 for blue, green and red), we estimate that achieving dN/dz errors that are at most 50% of the statistical errors will require 14000, 7500, and 1500 spectra for the blue, green and red samples. However, a smaller effort focused solely at low redshift could be just as effective for the red sample, since the low redshift tail is much more uncertain than the higher redshift dN/dz .

By measuring dN/dz across multiple fields, a spectroscopic followup program could constrain variations in dN/dz on the sky. Using the standard deviation of the COSMOS cross-match dN/dz , we estimate that we could measure a 5% shift in the mean dN/dz at 3σ with 1000 spectra per field for both the blue and green samples. For the red sample, with 400 spectra per field we could measure a 10% shift at 3σ .

B Simple HOD model for unWISE samples

When computing dN/dz using cross-correlations we assumed a scale-independent bias, and we found that in order for the cross-match and cross-correlation dN/dz to match, the biases

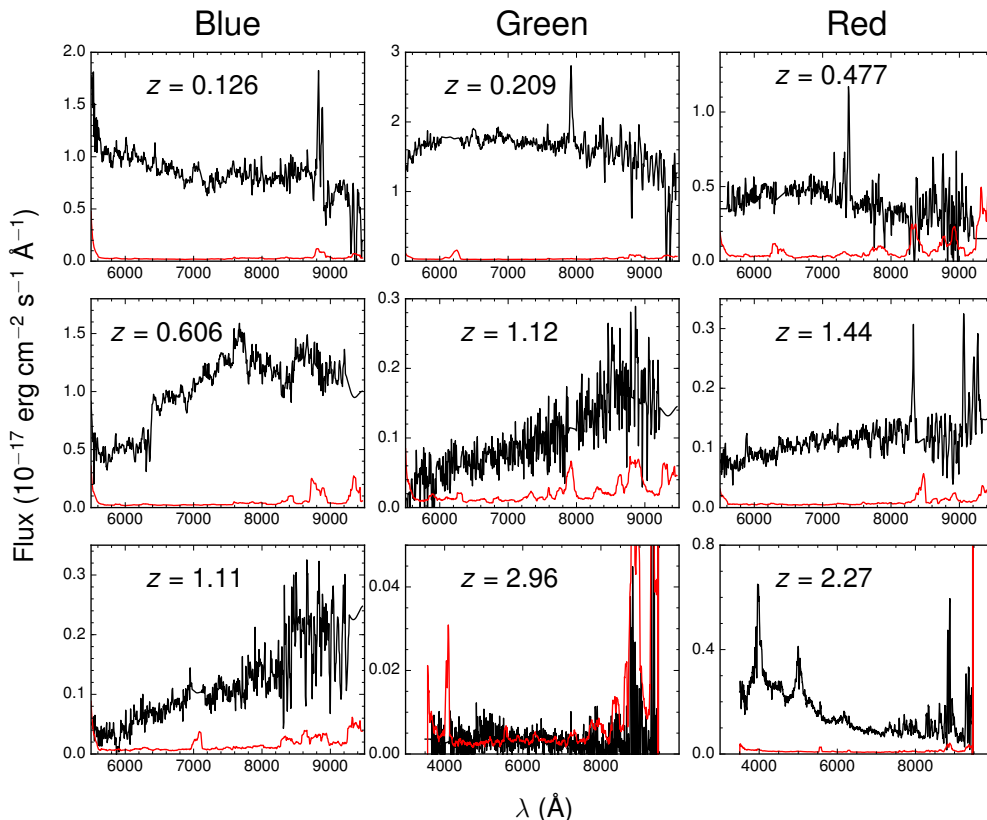


Figure 15. VVDS spectra from each of the three unWISE samples, with spectra in black and noise in red. For each of the three samples we display galaxies representative of the low, medium, and high portion of the redshift distribution. The highest redshift green and red galaxies are from VVDS-UltraDeep, which took spectra in both the blue and red grisms of VIMOS; all other galaxies are from VVDS-Deep, which only observed using the red grism.

needed to evolve relatively rapidly with redshift. In this Appendix we check whether this assumption and its implications are consistent with expectations from simple models of the manner in which galaxies populate dark matter halos.

A scale-independent bias is likely to be true on large, linear scales, but the extent to which this approximation is valid on the scales used in the dN/dz analysis is unclear. If the bias is scale-dependent, the redshift evolution of $b_{\text{sml,p}}$ may not match the redshift evolution of $b_{\text{lin,p}}$ (relevant for $C_{\ell}^{\kappa g}$ and C_{ℓ}^{gg}), potentially introducing a systematic bias. To investigate this issue we model the unWISE galaxies using a simple HOD applied to dark matter halos in N -body simulations, allowing us to study the scale and redshift dependence of the unWISE galaxy bias. Since our goal is modest, we simply use a 1-parameter family²⁸ of HODs based on ref. [111] with

$$\langle N_{\text{cen}} \rangle = \frac{1}{2} \left[1 + \text{erf} \left(\frac{\log_{10} M - \log_{10} M_{\text{cut}}}{\sqrt{2} \sigma_{\log_{10} M}} \right) \right] \quad ; \quad \sigma_{\log_{10} M} = 0.25 \quad (\text{B.1})$$

²⁸There is some evidence that HOD parameters scale approximately universally with number density, e.g. ref. [109]. A similar assumption is at the root of the ‘SHAM’ approximation [110].

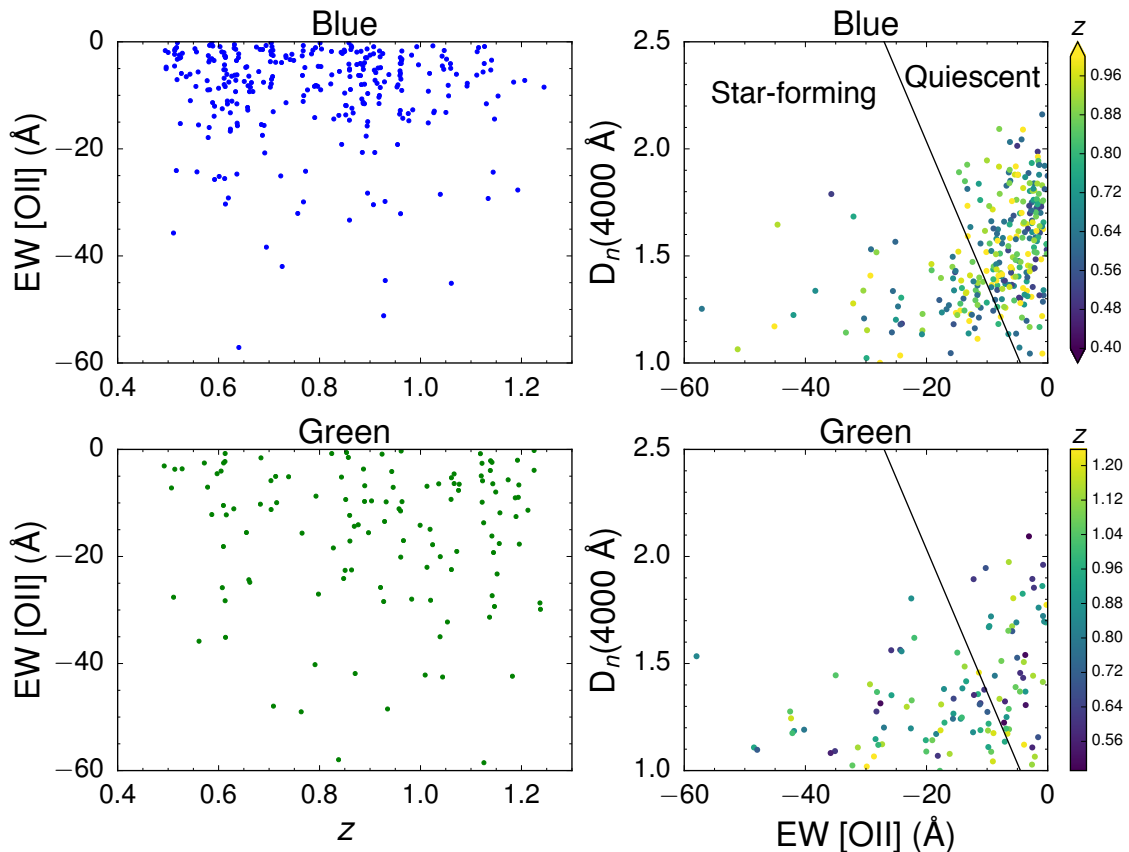


Figure 16. *Left:* From VVDS spectra, distribution of rest frame [OII] 3727 Å EW versus redshift for the blue sample (top) and green sample (bottom). *Right:* Distribution of [OII] 3727 Å EW versus $D_n(4000)$ to separate star forming and quiescent galaxies as in ref. [108]. Points are color-coded to represent redshift.

and

$$\langle N_{\text{sat}} \rangle = \left[\frac{M - 0.1M_{\text{cut}}}{15M_{\text{cut}}} \right]^{0.8}. \quad (\text{B.2})$$

The values of $\sigma_{\log_{10}M}$, and the power-law index and denominator in $\langle N_{\text{sat}} \rangle$ are typical of magnitude-selected galaxy samples and our final results are not very sensitive to them. The number density and large- and small-scale biases $b_{\text{HOD}}(z)$ can then be computed as a function of $\log_{10}M_{\text{cut}}$. We compute the comoving number density of unWISE galaxies from the COSMOS cross-match dN/dz (Section 5.1) and choose the cutoff mass M_c to match the abundance of each sample at all redshifts. The results are given in Table 8.

To reduce scatter, we averaged the results from halo catalogs generated from 4 simulations, each with 1280^3 particles in a $640 h^{-1}\text{Mpc}$ box, assuming ΛCDM with Planck 2014 cosmological parameters [112]. The simulations use the TreePM code of ref. [113], are described in section 2.1 of ref. [114], and are validated in ref. [115]. We consider friends-of-friends halos with linking length 0.168 of the mean interparticle spacing at four representative redshifts $z = 0.41, 1.00, 1.27$ and 1.78 . At each redshift we adjusted $\log_{10}M_{\text{cut}}$ as in Table 8 and measured the real-space correlation function by direct pair counting of the halos, hence ob-

z_{\min}	z_{\max}	LOWZ		CMASS		z_{\min}	z_{\max}	eBOSS Q		BOSS Q	
		$b_{\text{sml},s}$	σ_b	$b_{\text{sml},s}$	σ_b			$b_{\text{sml},s}$	σ_b	$b_{\text{sml},s}$	σ_b
0.00	0.05	1.34	0.0381			0.00	0.20				
0.05	0.10	1.37	0.0077			0.20	0.40				
0.10	0.15	1.52	0.0037	1.36	0.2698	0.40	0.60				
0.15	0.20	1.73	0.0045	2.82	0.2615	0.60	0.80				
0.20	0.25	1.89	0.0039	1.54	0.0796	0.80	1.00	1.72	0.2803		
0.25	0.30	2.01	0.0018	2.11	0.1489	1.00	1.20	2.03	0.0851		
0.30	0.35	2.01	0.0021	1.99	0.1054	1.20	1.40	2.05	0.0759		
0.35	0.40	2.06	0.0019	2.24	0.1674	1.40	1.60	2.35	0.0683		
0.40	0.45	2.25	0.0017	2.05	0.0020	1.60	1.80	2.32	0.0992		
0.45	0.50	2.46	0.0079	2.08	0.0006	1.80	2.00	2.89	0.1004		
0.50	0.55			2.06	0.0008	2.00	2.20	2.87	0.1548		
0.55	0.60			2.17	0.0007	2.20	2.40			4.33	0.0808
0.60	0.65			2.22	0.0010	2.40	2.60			3.72	0.1394
0.65	0.70			2.39	0.0022	2.60	2.80			4.27	0.3772
0.70	0.75			2.52	0.0090	2.80	3.00			4.30	1.2109
0.75	0.80			2.73	0.0872	3.00	3.20			4.30	1.1164
						3.20	3.40			5.33	1.9984

Table 7. Bias of the spectroscopic samples and the 1- σ error bar, as defined in Equation 5.9.

z	Blue		Green		Red	
	$\log_{10}(M_{\text{cut}})$	Abundance ($h^3 \text{ Mpc}^{-3}$)	$\log_{10}(M_{\text{cut}})$	Abundance ($h^3 \text{ Mpc}^{-3}$)	$\log_{10}(M_{\text{cut}})$	Abundance ($h^3 \text{ Mpc}^{-3}$)
0.41	12.25	3.44×10^{-3}	13.00	5.57×10^{-4}	13.50	1.39×10^{-4}
1.00	12.50	1.43×10^{-3}	12.75	7.19×10^{-4}	13.50	6.55×10^{-5}
1.27	13.25	1.11×10^{-4}	12.75	5.71×10^{-4}	13.50	4.26×10^{-5}
1.78			13.00	5.57×10^{-4}	13.50	1.39×10^{-4}

Table 8. Halos populated with the HOD of Eq. B.1 and Eq. B.2, at four output times. All HODs use $\sigma_{\log_{10} M} = 0.25$ decades, and $\log_{10} M_{\text{cut}}$ is then selected to roughly match the abundance of each unWISE sample at the specified redshift.

taining the projected correlation function, $w_p(R)$. We define the real-space bias as a function of scale

$$b(R) = \sqrt{w_p(R)/w_{p,\text{HF}}(R)} \quad (\text{B.3})$$

define b_{sml} with the same R^{-1} weighting as in Eq. 5.2:

$$b_{\text{sml}} = \int_{r_{\min}}^{r_{\max}} dR R^{-1} b(R) / \int_{r_{\min}}^{r_{\max}} dR R^{-1} \quad (\text{B.4})$$

and define $b_{\text{lin}} \equiv b(r = 40 h^{-1} \text{Mpc})$.

We find only mild departures from scale-independent bias at $2.5 < r_p < 10 h^{-1} \text{Mpc}$, but more significant deviations at smaller scales, in qualitative agreement with the spectroscopic cross-correlations (Figure 17). From the HOD-populated N -body autocorrelations, we find $b_{\text{sml}}/b_{\text{lin}} = 1.153$ for red at $z = 1.78$, the most massive and highest-redshift sample (Figure 18). To interpolate between the four measured points, we use a function of the form $b_{\text{sml}}/b_{\text{lin}} = 1 + Az^2$, with $A = 0.05$ for red and $A = 0.025$ for green and blue. The HOD has a milder

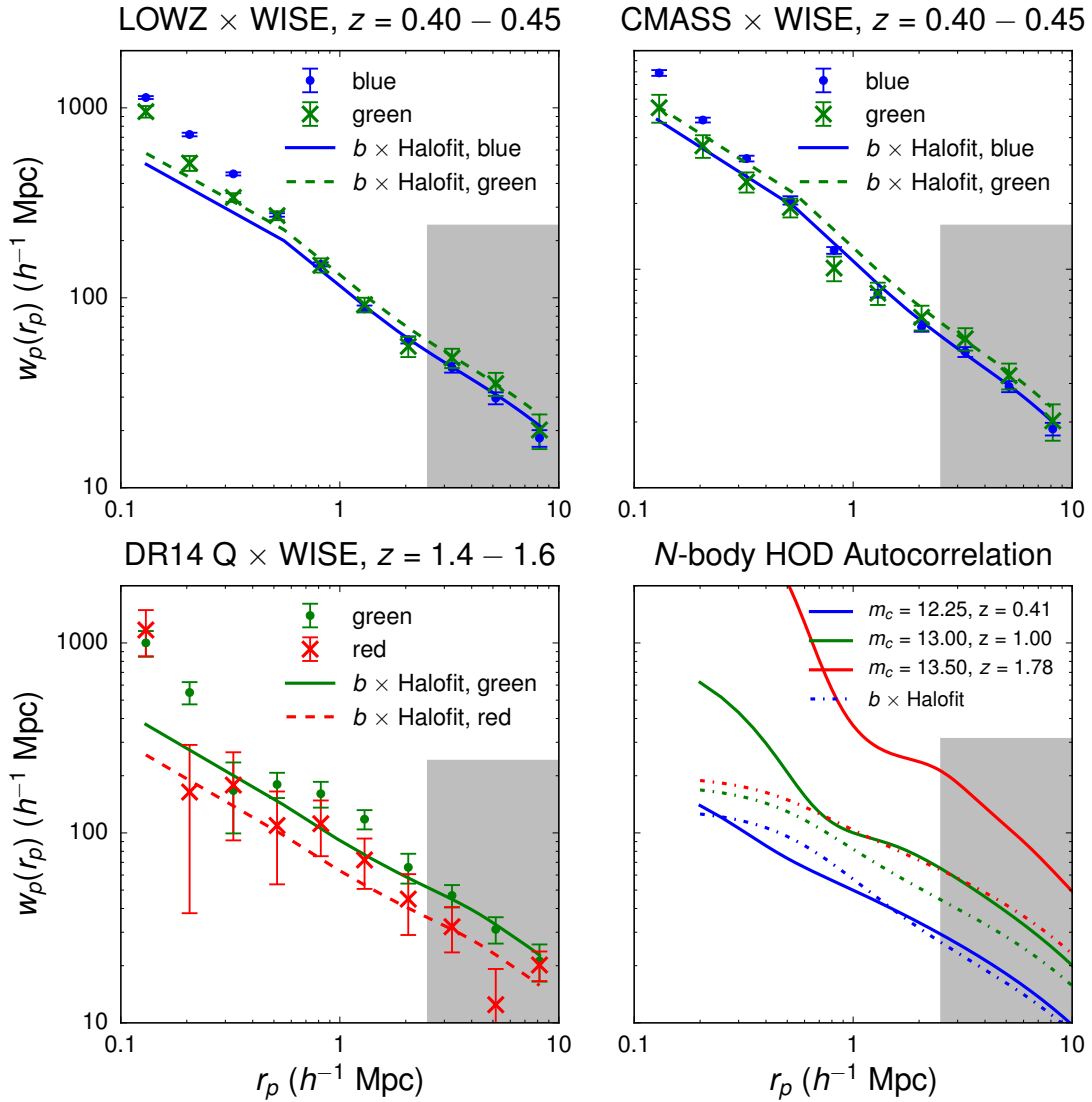


Figure 17. Cross-correlations between spectroscopic tracers and the unWISE galaxy samples, compared to a scale-independent bias times nonlinear correlation function fit to the points with $2.5 < r_p < 10 h^{-1} \text{ Mpc}$ (shaded region). Deviations from scale-independent bias are seen at $r_p < 2.5 h^{-1} \text{ Mpc}$, justifying our decision to use $2.5 < r_p < 10 h^{-1} \text{ Mpc}$ for the cross-correlation redshifts. *Lower right:* autocorrelation of galaxies populating halos in an N -body simulation according to Eq. B.1 and B.2 with $\sigma_{\log_{10} M} = 0.25$ decades. Redshifts and number densities are chosen to be roughly representative of the three unWISE samples. Since the lower right panel is an autocorrelation ($\propto b_{\text{unWISE}}^2$) while the other panels are cross-correlations ($\propto b_{\text{unWISE}}$), it has a much stronger scale-dependent bias at $z \sim 1.5$ (since the unWISE galaxies have larger and thus more scale-dependent bias than the quasars).

bias evolution than the data for the green and red samples (Figure 19). If we match the $z = 1.9$ clustering with a free number density, we find somewhat larger $b_{\text{sml}}/b_{\text{lin}}$ at $z = 1.9$, corresponding to $A \sim 0.15$ and 0.2 for green and red, respectively. When estimating the impact of this systematic in Section 7 and Figure 12, we therefore test both the fiducial value

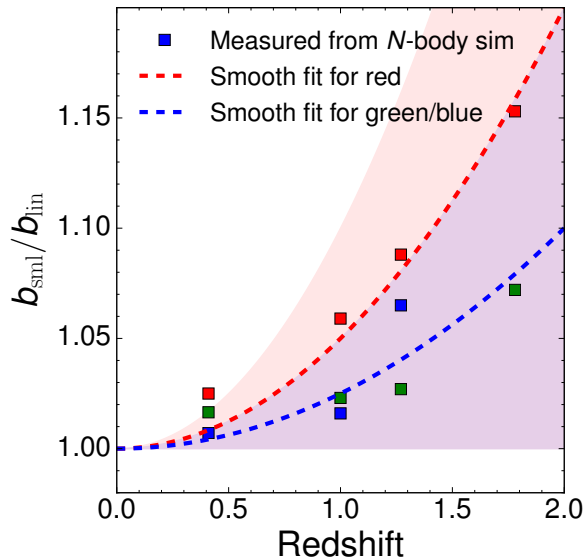


Figure 18. Ratio between b_{sml} and b_{lin} for HODs matched to the three unWISE samples at four representative redshifts in the N -body simulation. Dashed lines give interpolating functions $b_{\text{sml}}/b_{\text{lin}} = 1 + Az^2$ with separate values of A for red and blue/green; shaded regions represent uncertainty on A , accounting for uncertainty in the halo occupation of the unWISE galaxies.

of A , $A_{\text{fid}} = 0.025, 0.025, 0.1$ for blue, green and red; and the maximal value of A , $A_{\text{max}} = 0.1, 0.15, 0.2$ for blue, green and red.

To assess the compatibility of the cross-correlation and cross-match dN/dz , we compare the bias evolution of galaxies in the HOD, $b_{\text{HOD}}(z)$, to the observed bias evolution of the unWISE galaxies, $b_{\text{sml,p}}(z)$, in Figure 19. Using Equation 5.4, the COSMOS dN/dz , and s from Appendix C, we fit $b_{\text{sml,p}}(z)$ to $w(\theta)$ between 2.5 and $10 h^{-1}\text{Mpc}$. Consistency between the cross-match dN/dz and photometric-spectroscopic clustering (from which the cross-correlation dN/dz is derived) requires a steeply evolving galaxy bias (colored lines in Figure 19). In fact, the simple abundance-matched HOD yields a galaxy bias that is nearly as steep (Figure 19). We compare $b_{\text{sml,p}}(z)$ to $b_{\text{HOD}}(z)$ using the HOD above and one of three different mass function/mass-bias relationships (Tinker et al., [116, 117], Sheth, Mo and Tormen [118, 119], and Comparat et al. [120]). We consider both statistical errors on $b_{\text{sml,p}}$ from errors on the cross-correlation (errorbars in Figure 19), and errors on $b_{\text{sml,p}}$ from the uncertain dN/dz (gray band, giving 16th-84th percentile range from 100 draws from dN/dz). While the uncertainty in dN/dz will also affect the bias evolution of the abundance-matched halos by changing their comoving number density, this effect is smaller than the impact of uncertain dN/dz on $b_{\text{sml,p}}(z)$ because the bias is a shallow function of halo mass and thus number density.

For the blue sample, and for the red and green samples at $z > 1$, the measured bias evolution roughly agrees with the HOD prediction within the uncertainty from dN/dz . At $z < 1$, the bias of the red and green samples is significantly lower than the expectation from the HOD. However, both the red and green samples are bimodal, and it is possible that their low-redshift tails are not well-described by the HOD above. For instance, the low-redshift tails could consist of star-forming galaxies occupying halos with a duty cycle well below unity,

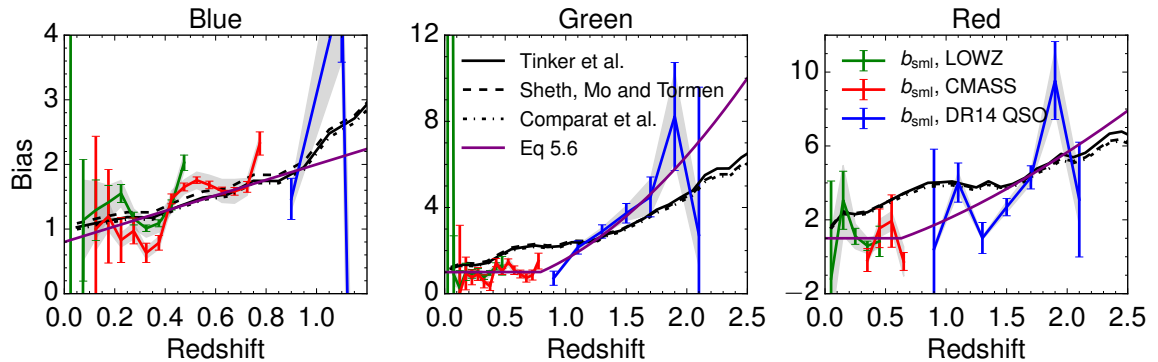


Figure 19. Bias, derived from $w(\theta)$ at $2.5 < r < 10 h^{-1}\text{Mpc}$ using Equation 5.4 and the COSMOS cross-match redshift distribution. Colored lines give the measured bias; black lines give the bias evolution for an HOD abundance-matched to the density of the WISE samples, with different line styles corresponding to different bias-number density prescriptions from the literature. Errorbars on the colored lines are from measurement errors on $w(\theta)$; the gray bands give the additional uncertainty from uncertain dN/dz , quantified by the 16th-84th percentile range from 100 samples of dN/dz . All fits to clustering include magnification bias using the fiducial values in Table 1 and Fig. 21.

such that at fixed abundance, the cutoff halo mass is much lower than the HOD above would predict, thus lowering the bias.

The rough agreement between $b_{\text{sml,p}}(z)$ and $b_{\text{HOD}}(z)$ for the abundance-matched halos shows that the combination of cross-correlation and cross-match redshifts yields a reasonable bias evolution. This result justifies our use of both the cross-correlation and cross-match redshifts in modelling $C_\ell^{\kappa g}$ and C_ℓ^{gg} , as it suggests they are consistent with each other.

C Response of the number density to magnification bias

The amplitude of the magnification bias term depends on the response of the galaxy density to magnification bias, $s \equiv d \log_{10} N/dm$, at the limiting magnitude of the survey. Since the completeness of WISE drops over a relatively large range, measurements of s are affected by incompleteness in WISE. This can be mitigated by restricting the sample to high ecliptic latitude, where the greater depth of coverage results in a fainter limiting magnitude.

Since the WISE galaxies are selected via a magnitude-dependent color cut, one cannot simply histogram them in W2 to determine s . Instead, we compute s by shifting the magnitudes of all WISE objects by 0.02 magnitudes and re-applying our selection criteria.

In Figure 20, we show s as a function of λ_{min} , where we sequentially remove all galaxies with $|\lambda| < \lambda_{\text{min}}$. We set the fiducial value of s at $\lambda_{\text{min}} = 60^\circ$.

We also require s for each of the spectroscopic samples in order to subtract the magnification bias contribution from \bar{w}_{sp} . We measure s by making all galaxies or quasars in the sample fainter by 0.1 magnitudes, applying the relevant selection criteria and measuring the change in number counts.

For LOWZ and CMASS, we use the color cuts described in Ref. [80]. This procedure assumes that every galaxy in the spectroscopic sample with perturbed photometry was also in the original sample; this is true for both CMASS and LOWZ (see Figures 3 and 4 in Ref. [80] for color-magnitude plots for LOWZ and CMASS, respectively).

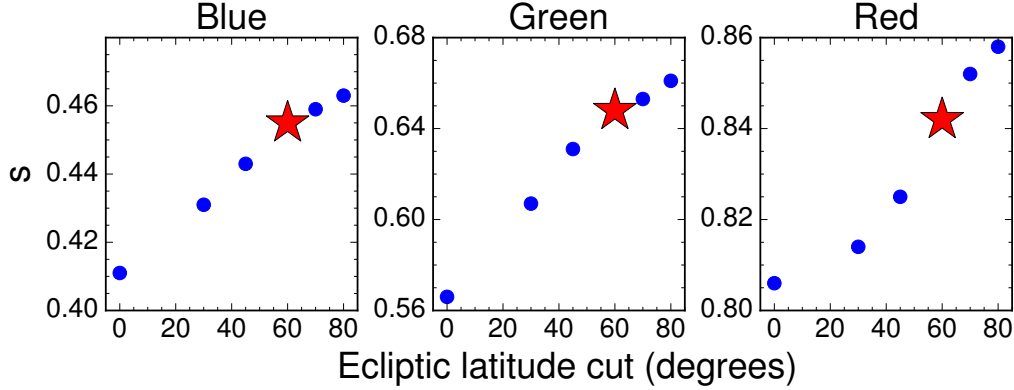


Figure 20. Dependence of s for the unWISE samples on ecliptic latitude. Each point shows $s(\lambda_{\min})$ measured using galaxies with ecliptic $|\lambda| > \lambda_{\min}$. The starred point gives the fiducial value of s , using $\lambda_{\min} = 60^\circ$.

DR12 quasars are selected as point sources with $g < 22$ or $r < 21.85$, $i > 17.8$, and XDQSO “mid- z ” quasar probability (i.e. probability the object is a $2.2 < z < 3.5$ quasar) > 0.424 [121, 122]. When we make the quasars fainter by 0.1 magnitudes, we estimate the number of quasars that would be spuriously categorized as extended using the completeness of SDSS star-galaxy separation as a function of r band magnitude [123].²⁹ Unlike the color cuts used for the BOSS galaxies, with the more complicated XDQSO color cut it is possible that quasars could be excluded from the original targeting but included when the photometry is made fainter by 0.1 magnitudes. To estimate the occurrence of such objects, we use the BOSS BONUS sample of non-uniformly-selected quasars, which are not suitable for quasar clustering analyses but are $\sim 2\times$ as abundant as the CORE sample that we do use. Since BONUS quasars are not selected using XDQSO, they may have mid- z quasar probability < 0.424 but “scatter into” our fainter sample.

For DR14 quasars, we follow a similar procedure as for DR12 quasars, applying the selection criteria of Ref. [86]. However, we lack a similarly deep quasar sample (like BONUS in DR12) to determine the number of quasars that scatter into the DR14 selection criteria when the quasar photometry becomes fainter. Based on the number of quasars that scattered into the DR12 quasar selection, we estimate an additional systematic error of $\Delta s \sim 0.1 - 0.2$ for the DR14 quasars.

We plot the resulting s in Figure 21, and use them to remove magnification bias from \bar{w} . For z beyond the range shown in Figure 21, we assume s is a constant function, using the nearest point for which we have a measurement of s .

D Galaxy-galaxy cross spectra

In Figure 22 we show the cross-spectra between the different galaxy samples. We use the fiducial cross-correlation dN/dz and $b_{\text{cross}}^{\text{eff}}$ for the theory calculation. Additionally, we fit a shot-noise term, and find good agreement between the expectation and the data once the uncertainty on dN/dz is taken into account. For red cross blue the shot noise term is negligible, but for blue cross green and blue cross red, we find shot noise values of 6.22×10^{-9} and 4.67×10^{-8} , respectively. Shot noise can arise in a cross-correlation if some of the objects

²⁹<https://classic.sdss.org/dr7/products/general/stargalsep.html>

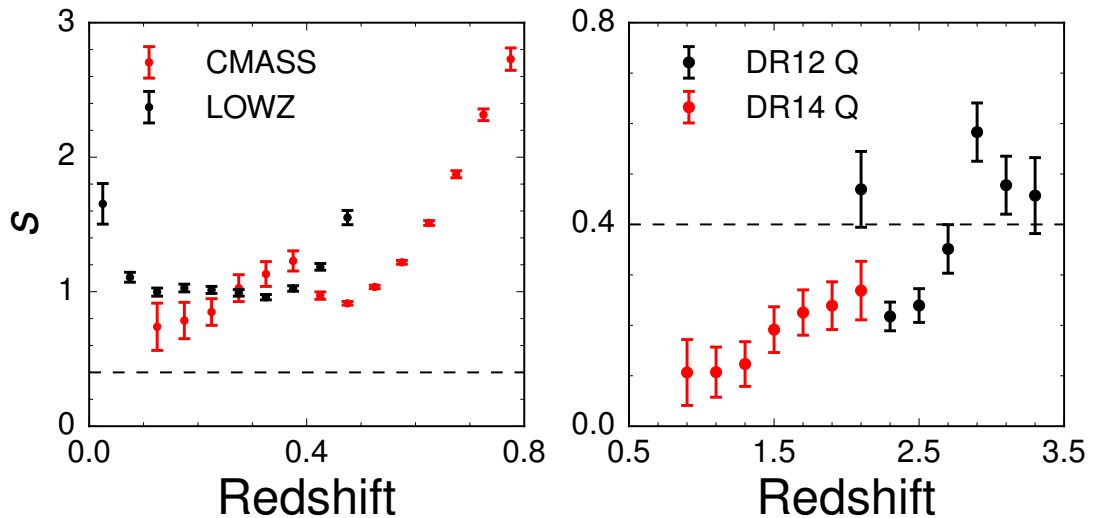


Figure 21. Response of galaxy number density to magnification for spectroscopic samples. Error bars are computed as $\Delta s = (\log_{10} N - \log_{10}(N - \sqrt{N}))/\Delta m$. Dashed line indicates $s = 0.4$, where magnification bias makes no contribution to the observed clustering.

in the two samples occupy the same halo, with density \bar{n}_{common} . The cross shot-noise is then given by

$$\text{Shot Noise} = \frac{\bar{n}_{\text{common}}}{\bar{n}_1 \bar{n}_2} \quad (\text{D.1})$$

Using the fitted shot noise for each sample from Table 4, we find $\bar{n}_{\text{common}} = 130 \text{ deg}^{-2}$ for blue cross green and 41 deg^{-2} for green cross red. This implies that 3.8% (7.0%) of the blue (green) sample lives in the same halo as a green (blue) object, and 2.2% (28.5%) of the green (red) sample lives in the same halo as a red (green) object.

We create a simple “joint HOD” to understand the cross shot-noise. Rather than assume that every halo well above M_{cut} hosts a central galaxy, we instead assume that some halos host red centrals and other halos host green centrals; i.e. we multiply N_{cen} by f_{green} or f_{red} where $f_{\text{green}} + f_{\text{red}} = 1$, and do not modify N_{sat} . We then ask what fraction of red galaxies host a green satellite. If $f_{\text{green}} = f_{\text{red}} = 0.5$, we find that 26.3% of red galaxies host at least one green satellite. The common fraction remains similar at 15-25% if we change some aspects of this toy model (i.e. increase f_{green} to 0.9; add a linear ramp where halos transition from hosting green galaxies at low redshift to red galaxies at high redshift; or multiply N_{sat} by 0.5 for both green and red to preserve the total number of satellites).

References

- [1] A. Lewis and A. Challinor, *Weak gravitational lensing of the CMB*, *PhysRep* **429** (2006) 1 [[astro-ph/0601594](#)].
- [2] D. Hanson, A. Challinor and A. Lewis, *Weak lensing of the CMB*, *General Relativity and Gravitation* **42** (2010) 2197 [[0911.0612](#)].
- [3] W. Hu, *Power spectrum tomography with weak lensing*, *Astrophys. J.* **522** (1999) L21 [[astro-ph/9904153](#)].

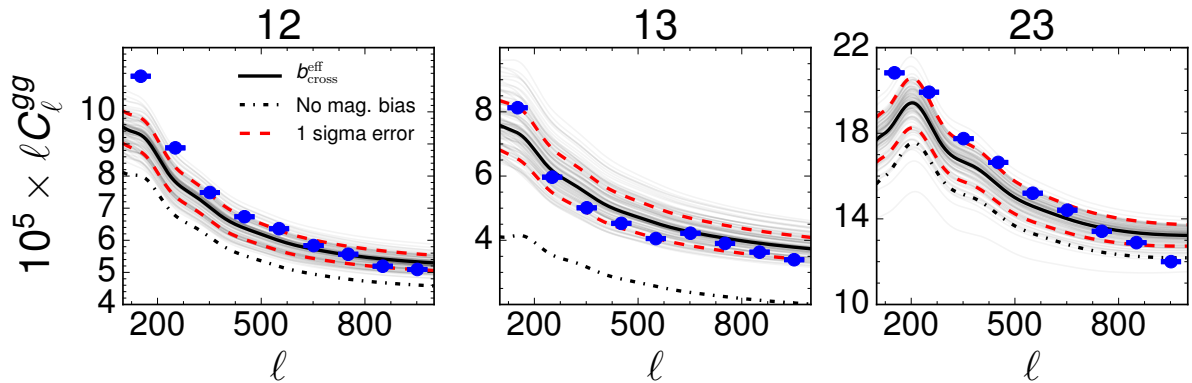


Figure 22. Galaxy-galaxy cross-spectra between the different samples. The solid black line gives the predicted theory curve using $b_{\text{cross}}^{\text{eff}}$, and the dot-dashed black line gives the predicted theory curve with no magnification bias included. Gray lines show C_{ℓ}^{gg} from 100 realizations of dN/dz (with bias modified from the best-fit $b_{\text{cross}}^{\text{eff}}$ in Table 4 to fit C_{ℓ}^{gg} for a given dN/dz); and dashed red lines show 1σ uncertainty in C_{ℓ}^{gg} , with contributions both from uncertain dN/dz and from statistical errors on $b_{\text{cross}}^{\text{eff}}$. Uncertainty on C_{ℓ}^{gg} for dN/dz from the two halves of the sky is comparable to the 1σ uncertainty. In all cases, a cross shot-noise term is fit to the data and also included in the theory curves.

- [4] W. Hu, *Dark energy and matter evolution from lensing tomography*, *Phys. Rev.* **D66** (2002) 083515 [[astro-ph/0208093](#)].
- [5] K. M. Smith, O. Zahn and O. Dore, *Detection of Gravitational Lensing in the Cosmic Microwave Background*, *Phys. Rev.* **D76** (2007) 043510 [[0705.3980](#)].
- [6] C. M. Hirata, S. Ho, N. Padmanabhan, U. Seljak and N. A. Bahcall, *Correlation of CMB with large-scale structure: II. Weak lensing*, *Phys. Rev.* **D78** (2008) 043520 [[0801.0644](#)].
- [7] B. D. Sherwin et al., *The Atacama Cosmology Telescope: Cross-Correlation of CMB Lensing and Quasars*, *Phys. Rev.* **D86** (2012) 083006 [[1207.4543](#)].
- [8] L. E. Bleem et al., *A Measurement of the Correlation of Galaxy Surveys with CMB Lensing Convergence Maps from the South Pole Telescope*, *Astrophys. J.* **753** (2012) L9 [[1203.4808](#)].
- [9] Planck Collaboration, P. A. R. Ade, N. Aghanim, C. Armitage-Caplan, M. Arnaud, M. Ashdown et al., *Planck 2013 results. XVII. Gravitational lensing by large-scale structure*, *A&A* **571** (2014) A17 [[1303.5077](#)].
- [10] Y. Omori and G. Holder, *Cross-Correlation of CFHTLenS Galaxy Number Density and Planck CMB Lensing*, *arXiv e-prints* (2015) arXiv:1502.03405 [[1502.03405](#)].
- [11] R. Allison, S. N. Lindsay, B. D. Sherwin, F. de Bernardis, J. R. Bond, E. Calabrese et al., *The Atacama Cosmology Telescope: measuring radio galaxy bias through cross-correlation with lensing*, *MNRAS* **451** (2015) 849 [[1502.06456](#)].
- [12] F. Bianchini, P. Bielewicz, A. Lapi, J. Gonzalez-Nuevo, C. Baccigalupi, G. de Zotti et al., *Cross-correlation between the CMB Lensing Potential Measured by Planck and High- z Submillimeter Galaxies Detected by the Herschel-Atlas Survey*, *ApJ* **802** (2015) 64 [[1410.4502](#)].
- [13] E. Baxter, J. Clampitt, T. Giannantonio, S. Dodelson, B. Jain, D. Huterer et al., *Joint measurement of lensing-galaxy correlations using SPT and DES SV data*, *MNRAS* **461** (2016) 4099 [[1602.07384](#)].

- [14] T. Giannantonio, P. Fosalba, R. Cawthon, Y. Omori, M. Crocce, F. Elsner et al., *CMB lensing tomography with the DES Science Verification galaxies*, *MNRAS* **456** (2016) 3213 [1507.05551].
- [15] Y. Omori, T. Giannantonio, A. Porredon, E. Baxter, C. Chang, M. Crocce et al., *Dark Energy Survey Year 1 Results: tomographic cross-correlations between DES galaxies and CMB lensing from SPT+Planck*, *arXiv e-prints* (2018) arXiv:1810.02342 [1810.02342].
- [16] G. A. Marques and A. Bernui, *Tomographic analyses of the CMB lensing and galaxy clustering to probe the linear structure growth*, 1908.04854.
- [17] E. F. Schlafly, A. M. Meisner and G. M. Green, *The unWISE Catalog: Two Billion Infrared Sources from Five Years of WISE Imaging*, *The Astrophysical Journal Supplement Series* **240** (2019) 30 [1901.03337].
- [18] E. L. Wright, P. R. M. Eisenhardt, A. K. Mainzer, M. E. Ressler, R. M. Cutri, T. Jarrett et al., *The Wide-field Infrared Survey Explorer (WISE): Mission Description and Initial On-orbit Performance*, *AJ* **140** (2010) 1868 [1008.0031].
- [19] Gaia Collaboration, T. Prusti, J. H. J. de Bruijne, A. G. A. Brown, A. Vallenari, C. Babusiaux et al., *The Gaia mission*, *A&A* **595** (2016) A1 [1609.04153].
- [20] S. Ferraro, B. D. Sherwin and D. N. Spergel, *WISE measurement of the integrated Sachs-Wolfe effect*, *PRD* **91** (2015) 083533 [1401.1193].
- [21] S. Ferraro, J. C. Hill, N. Battaglia, J. Liu and D. N. Spergel, *Kinematic Sunyaev-Zel'dovich effect with projected fields. II. Prospects, challenges, and comparison with simulations*, *Phys. Rev. D* **94** (2016) 123526 [1605.02722].
- [22] J. C. Hill, S. Ferraro, N. Battaglia, J. Liu and D. N. Spergel, *Kinematic Sunyaev-Zel'dovich Effect with Projected Fields: A Novel Probe of the Baryon Distribution with Planck, WMAP, and WISE Data*, *Phys. Rev. Lett.* **117** (2016) 051301 [1603.01608].
- [23] A. J. Shajib and E. L. Wright, *Measurement of the integrated Sachs-Wolfe effect using the AllWISE data release*, *Astrophys. J.* **827** (2016) 116 [1604.03939].
- [24] J. A. Peacock and M. Bilicki, *Wide-area tomography of CMB lensing and the growth of cosmological density fluctuations*, *MNRAS* **481** (2018) 1133 [1805.11525].
- [25] Planck Collaboration, N. Aghanim, Y. Akrami, M. Ashdown, J. Aumont, C. Baccigalupi et al., *Planck 2018 results. VIII. Gravitational lensing*, *ArXiv e-prints* (2018) [1807.06210].
- [26] A. Krolewski, S. Ferraro, E. Schlafly and M. J. White, *In Preparation* (2019), .
- [27] Planck Collaboration, N. Aghanim, Y. Akrami, M. Ashdown, J. Aumont, C. Baccigalupi et al., *Planck 2018 results. VI. Cosmological parameters*, *arXiv e-prints* (2018) arXiv:1807.06209 [1807.06209].
- [28] W. Hu and T. Okamoto, *Mass Reconstruction with Cosmic Microwave Background Polarization*, *ApJ* **574** (2002) 566 [astro-ph/0111606].
- [29] K. M. Górski, E. Hivon, A. J. Banday, B. D. Wand elt, F. K. Hansen, M. Reinecke et al., *HEALPix: A Framework for High-Resolution Discretization and Fast Analysis of Data Distributed on the Sphere*, *ApJ* **622** (2005) 759 [astro-ph/0409513].
- [30] E. Schaan and S. Ferraro, *Foreground-Immune Cosmic Microwave Background Lensing with Shear-Only Reconstruction*, *Phys. Rev. Lett.* **122** (2019) 181301 [1804.06403].
- [31] M. S. Madhavacheril and J. C. Hill, *Mitigating Foreground Biases in CMB Lensing Reconstruction Using Cleaned Gradients*, *Phys. Rev. D* **98** (2018) 023534 [1802.08230].
- [32] A. van Engelen, S. Bhattacharya, N. Sehgal, G. P. Holder, O. Zahn and D. Nagai, *CMB Lensing Power Spectrum Biases from Galaxies and Clusters using High-angular Resolution Temperature Maps*, *Astrophys. J.* **786** (2014) 13 [1310.7023].

- [33] S. J. Osborne, D. Hanson and O. Doré, *Extragalactic Foreground Contamination in Temperature-based CMB Lens Reconstruction*, *JCAP* **1403** (2014) 024 [[1310.7547](#)].
- [34] A. Mainzer, J. Bauer, T. Grav, J. Masiero, R. M. Cutri, J. Dailey et al., *Preliminary Results from NEOWISE: An Enhancement to the Wide-field Infrared Survey Explorer for Solar System Science*, *ApJ* **731** (2011) 53 [[1102.1996](#)].
- [35] R. M. Cutri, E. L. Wright, T. Conrow, J. W. Fowler, P. R. M. Eisenhardt, C. Grillmair et al., *Explanatory Supplement to the AllWISE Data Release Products*, tech. rep., Nov, 2013.
- [36] A. Mainzer, J. Bauer, R. M. Cutri, T. Grav, J. Masiero, R. Beck et al., *Initial Performance of the NEOWISE Reactivation Mission*, *ApJ* **792** (2014) 30 [[1406.6025](#)].
- [37] A. M. Meisner, D. Lang and D. J. Schlegel, *Full-depth Coadds of the WISE and First-year NEOWISE-reactivation Images*, *AJ* **153** (2017) 38 [[1603.05664](#)].
- [38] A. M. Meisner, D. Lang and D. J. Schlegel, *Deep Full-sky Coadds from Three Years of WISE and NEOWISE Observations*, *AJ* **154** (2017) 161 [[1705.06746](#)].
- [39] A. M. Meisner, D. Lang and D. J. Schlegel, *Another unWISE Update: The Deepest Ever Full-sky Maps at 3-5 μm* , *Research Notes of the American Astronomical Society* **2** (2018) 1 [[1801.03566](#)].
- [40] E. F. Schlafly, G. M. Green, D. Lang, T. Daylan, D. P. Finkbeiner, A. Lee et al., *The DECam Plane Survey: Optical Photometry of Two Billion Objects in the Southern Galactic Plane*, *The Astrophysical Journal Supplement Series* **234** (2018) 39 [[1710.01309](#)].
- [41] C. Laigle, H. J. McCracken, O. Ilbert, B. C. Hsieh, I. Davidzon, P. Capak et al., *The COSMOS2015 Catalog: Exploring the $1 < z < 6$ Universe with Half a Million Galaxies*, *ApJS* **224** (2016) 24 [[1604.02350](#)].
- [42] Gaia Collaboration, A. G. A. Brown, A. Vallenari, T. Prusti, J. H. J. de Bruijne, C. Babusiaux et al., *Gaia Data Release 2. Summary of the contents and survey properties*, *A&A* **616** (2018) A1 [[1804.09365](#)].
- [43] D. Makarov, P. Prugniel, N. Terekhova, H. Courtois and I. Vauglin, *HyperLEDA. III. The catalogue of extragalactic distances*, *A&A* **570** (2014) A13 [[1408.3476](#)].
- [44] A. Acker, F. Cuisinier, B. Stenholm and A. Terzan, *New planetary nebulae in the galactic bulge.*, *A&A* **264** (1992) 217.
- [45] D. N. Limber, *The Analysis of Counts of the Extragalactic Nebulae in Terms of a Fluctuating Density Field.*, *ApJ* **117** (1953) 134.
- [46] M. Loverde and N. Afshordi, *Extended Limber approximation*, *PRD* **78** (2008) 123506 [[0809.5112](#)].
- [47] R. Takahashi, M. Sato, T. Nishimichi, A. Taruya and M. Oguri, *Revising the Halofit Model for the Nonlinear Matter Power Spectrum*, *ApJ* **761** (2012) 152 [[1208.2701](#)].
- [48] D. Blas, J. Lesgourgues and T. Tram, *The Cosmic Linear Anisotropy Solving System (CLASS). Part II: Approximation schemes*, *Journal of Cosmology and Astro-Particle Physics* **2011** (2011) 034 [[1104.2933](#)].
- [49] C. Modi, M. White and Z. Vlah, *Modeling CMB lensing cross correlations with CLEFT*, *JCAP* **8** (2017) 009 [[1706.03173](#)].
- [50] M. Costanzi, F. Villaescusa-Navarro, M. Viel, J.-Q. Xia, S. Borgani, E. Castorina et al., *Cosmology with massive neutrinos III: the halo mass function and an application to galaxy clusters*, *Journal of Cosmology and Astro-Particle Physics* **2013** (2013) 012 [[1311.1514](#)].
- [51] F. Villaescusa-Navarro, F. Marulli, M. Viel, E. Branchini, E. Castorina, E. Sefusatti et al., *Cosmology with massive neutrinos I: towards a realistic modeling of the relation between*

matter, haloes and galaxies, *Journal of Cosmology and Astro-Particle Physics* **2014** (2014) 011 [1311.0866].

- [52] E. Castorina, E. Sefusatti, R. K. Sheth, F. Villaescusa-Navarro and M. Viel, *Cosmology with massive neutrinos II: on the universality of the halo mass function and bias*, *Journal of Cosmology and Astro-Particle Physics* **2014** (2014) 049 [1311.1212].
- [53] E. Castorina, C. Carbone, J. Bel, E. Sefusatti and K. Dolag, *DEMNUi: the clustering of large-scale structures in the presence of massive neutrinos*, *Journal of Cosmology and Astro-Particle Physics* **2015** (2015) 043 [1505.07148].
- [54] S. Vagnozzi, T. Brinckmann, M. Archidiacono, K. Freese, M. Gerbino, J. Lesgourgues et al., *Bias due to neutrinos must not uncorrect'd go*, *Journal of Cosmology and Astro-Particle Physics* **2018** (2018) 001 [1807.04672].
- [55] E. Hivon, K. M. Górski, C. B. Netterfield, B. P. Crill, S. Prunet and F. Hansen, *MASTER of the Cosmic Microwave Background Anisotropy Power Spectrum: A Fast Method for Statistical Analysis of Large and Complex Cosmic Microwave Background Data Sets*, *ApJ* **567** (2002) 2 [astro-ph/0105302].
- [56] D. Alonso, J. Sanchez and A. Slosar, *A unified pseudo- C_ℓ framework*, *ArXiv e-prints* (2018) [1809.09603].
- [57] G. Efstathiou, *Myths and truths concerning estimation of power spectra*, *Mon. Not. Roy. Astron. Soc.* **349** (2004) 603 [astro-ph/0307515].
- [58] C. García-García, D. Alonso and E. Bellini, *Disconnected pseudo- C_ℓ covariances for projected large-scale structure data*, 1906.11765.
- [59] J. A. Newman, *Calibrating Redshift Distributions beyond Spectroscopic Limits with Cross-Correlations*, *ApJ* **684** (2008) 88 [0805.1409].
- [60] M. McQuinn and M. White, *On using angular cross-correlations to determine source redshift distributions*, *MNRAS* **433** (2013) 2857 [1302.0857].
- [61] B. Ménard, R. Scranton, S. Schmidt, C. Morrison, D. Jeong, T. Budavari et al., *Clustering-based redshift estimation: method and application to data*, *arXiv e-prints* (2013) [1303.4722].
- [62] H. Aihara, R. Armstrong, S. Bickerton, J. Bosch, J. Coupon, H. Furusawa et al., *First data release of the Hyper Suprime-Cam Subaru Strategic Program*, *PASJ* **70** (2018) S8 [1702.08449].
- [63] M. Tanaka, J. Coupon, B.-C. Hsieh, S. Mineo, A. J. Nishizawa, J. Speagle et al., *Photometric redshifts for Hyper Suprime-Cam Subaru Strategic Program Data Release 1*, *PASJ* **70** (2018) S9 [1704.05988].
- [64] S. J. Schmidt, B. Ménard, R. Scranton, C. Morrison and C. K. McBride, *Recovering redshift distributions with cross-correlations: pushing the boundaries*, *MNRAS* **431** (2013) 3307 [1303.0292].
- [65] S. J. Schmidt, B. Ménard, R. Scranton, C. B. Morrison, M. Rahman and A. M. Hopkins, *Inferring the redshift distribution of the cosmic infrared background*, *MNRAS* **446** (2015) 2696 [1407.0031].
- [66] M. Rahman, B. Ménard, R. Scranton, S. J. Schmidt and C. B. Morrison, *Clustering-based redshift estimation: comparison to spectroscopic redshifts*, *MNRAS* **447** (2015) 3500 [1407.7860].
- [67] M. Rahman, A. J. Mendez, B. Ménard, R. Scranton, S. J. Schmidt, C. B. Morrison et al., *Exploring the SDSS photometric galaxies with clustering redshifts*, *MNRAS* **460** (2016) 163 [1512.03057].

- [68] M. Rahman, B. Ménard and R. Scranton, *Exploring the 2MASS extended and point source catalogues with clustering redshifts*, *MNRAS* **457** (2016) 3912 [1508.03046].
- [69] V. Scottez, Y. Mellier, B. R. Granett, T. Moutard, M. Kilbinger, M. Scodreggio et al., *Clustering-based redshift estimation: application to VIPERS/CFHTLS*, *MNRAS* **462** (2016) 1683 [1605.05501].
- [70] V. Scottez, A. Benoit-Lévy, J. Coupon, O. Ilbert and Y. Mellier, *Testing the accuracy of clustering redshifts with simulations*, *MNRAS* **474** (2018) 3921 [1705.02629].
- [71] A. Johnson, C. Blake, A. Amon, T. Erben, K. Glazebrook, J. Harnois-Deraps et al., *2dFLenS and KiDS: determining source redshift distributions with cross-correlations*, *MNRAS* **465** (2017) 4118 [1611.07578].
- [72] C. Davis, E. Rozo, A. Roodman, A. Alarcon, R. Cawthon, M. Gatti et al., *Cross-correlation redshift calibration without spectroscopic calibration samples in DES Science Verification Data*, *MNRAS* **477** (2018) 2196 [1707.08256].
- [73] R. Cawthon, C. Davis, M. Gatti, P. Vielzeuf, J. Elvin-Poole, E. Rozo et al., *Dark Energy Survey Year 1 Results: calibration of redMaGiC redshift distributions in DES and SDSS from cross-correlations*, *MNRAS* **481** (2018) 2427 [1712.07298].
- [74] M. Gatti, P. Vielzeuf, C. Davis, R. Cawthon, M. M. Rau, J. DeRose et al., *Dark Energy Survey Year 1 results: cross-correlation redshifts - methods and systematics characterization*, *MNRAS* **477** (2018) 1664 [1709.00992].
- [75] D. J. Bates, R. Tojeiro, J. A. Newman, V. Gonzalez-Perez, J. Comparat, D. P. Schneider et al., *Mass functions, luminosity functions, and completeness measurements from clustering redshifts*, *MNRAS* **486** (2019) 3059 [1810.01767].
- [76] A. J. Mead, J. A. Peacock, C. Heymans, S. Joudaki and A. F. Heavens, *An accurate halo model for fitting non-linear cosmological power spectra and baryonic feedback models*, *MNRAS* **454** (2015) 1958 [1505.07833].
- [77] M. Davis and P. J. E. Peebles, *A survey of galaxy redshifts. V - The two-point position and velocity correlations*, *ApJ* **267** (1983) 465.
- [78] I. Pâris, P. Petitjean, N. P. Ross, A. D. Myers, É. Aubourg, A. Streblyanska et al., *The Sloan Digital Sky Survey Quasar Catalog: Twelfth data release*, *A&A* **597** (2017) A79 [1608.06483].
- [79] M. Ata, F. Baumgarten, J. Bautista, F. Beutler, D. Bizyaev, M. R. Blanton et al., *The clustering of the SDSS-IV extended Baryon Oscillation Spectroscopic Survey DR14 quasar sample: first measurement of baryon acoustic oscillations between redshift 0.8 and 2.2*, *MNRAS* **473** (2018) 4773 [1705.06373].
- [80] B. Reid, S. Ho, N. Padmanabhan, W. J. Percival, J. Tinker, R. Tojeiro et al., *SDSS-III Baryon Oscillation Spectroscopic Survey Data Release 12: galaxy target selection and large-scale structure catalogues*, *MNRAS* **455** (2016) 1553 [1509.06529].
- [81] S. Eftekharzadeh, A. D. Myers, M. White, D. H. Weinberg, D. P. Schneider, Y. Shen et al., *Clustering of intermediate redshift quasars using the final SDSS III-BOSS sample*, *MNRAS* **453** (2015) 2779 [1507.08380].
- [82] J. Bovy, J. F. Hennawi, D. W. Hogg, A. D. Myers, J. A. Kirkpatrick, D. J. Schlegel et al., *Think Outside the Color Box: Probabilistic Target Selection and the SDSS-XDQSO Quasar Targeting Catalog*, *ApJ* **729** (2011) 141 [1011.6392].
- [83] M. White, A. D. Myers, N. P. Ross, D. J. Schlegel, J. F. Hennawi, Y. Shen et al., *The clustering of intermediate-redshift quasars as measured by the Baryon Oscillation Spectroscopic Survey*, *MNRAS* **424** (2012) 933 [1203.5306].

- [84] S. Alam, M. Ata, S. Bailey, F. Beutler, D. Bizyaev, J. A. Blazek et al., *The clustering of galaxies in the completed SDSS-III Baryon Oscillation Spectroscopic Survey: cosmological analysis of the DR12 galaxy sample*, *MNRAS* **470** (2017) 2617 [1607.03155].
- [85] A. J. Ross, F. Beutler, C.-H. Chuang, M. Pellejero-Ibanez, H.-J. Seo, M. Vargas-Magaña et al., *The clustering of galaxies in the completed SDSS-III Baryon Oscillation Spectroscopic Survey: observational systematics and baryon acoustic oscillations in the correlation function*, *MNRAS* **464** (2017) 1168 [1607.03145].
- [86] A. D. Myers, N. Palanque-Delabrouille, A. Prakash, I. Pâris, C. Yeche, K. S. Dawson et al., *The SDSS-IV Extended Baryon Oscillation Spectroscopic Survey: Quasar Target Selection*, *ApJS* **221** (2015) 27 [1508.04472].
- [87] J. M. Loh and M. L. Stein, *Bootstrapping a spatial point process*, *Statistica Sinica* **14** (2004) 69.
- [88] J. M. Loh, *A Valid and Fast Spatial Bootstrap for Correlation Functions*, *ApJ* **681** (2008) 726.
- [89] P. Norberg, C. M. Baugh, E. Gaztañaga and D. J. Croton, *Statistical analysis of galaxy surveys - I. Robust error estimation for two-point clustering statistics*, *MNRAS* **396** (2009) 19 [0810.1885].
- [90] A. D. Myers, P. J. Outram, T. Shanks, B. J. Boyle, S. M. Croom, N. S. Loaring et al., *On statistical lensing and the anticorrelation between 2dF QSOs and foreground galaxies*, *MNRAS* **359** (2005) 741 [astro-ph/0502481].
- [91] N. P. Ross, Y. Shen, M. A. Strauss, D. E. Vanden Berk, A. J. Connolly, G. T. Richards et al., *Clustering of Low-redshift ($z < 2.2$) Quasars from the Sloan Digital Sky Survey*, *ApJ* **697** (2009) 1634 [0903.3230].
- [92] A. J. Ross, W. J. Percival, A. G. Sánchez, L. Samushia, S. Ho, E. Kazin et al., *The clustering of galaxies in the SDSS-III Baryon Oscillation Spectroscopic Survey: analysis of potential systematics*, *MNRAS* **424** (2012) 564 [1203.6499].
- [93] A. J. Ross, L. Samushia, A. Burden, W. J. Percival, R. Tojeiro, M. Manera et al., *The clustering of galaxies in the SDSS-III DR10 Baryon Oscillation Spectroscopic Survey: no detectable colour dependence of distance scale or growth rate measurements*, *MNRAS* **437** (2014) 1109 [1310.1106].
- [94] P. Laurent, S. Eftekharzadeh, J.-M. Le Goff, A. Myers, E. Burtin, M. White et al., *Clustering of quasars in SDSS-IV eBOSS: study of potential systematics and bias determination*, *JCAP* **7** (2017) 017 [1705.04718].
- [95] C.-H. Chuang, M. Pellejero-Ibanez, S. Rodríguez-Torres, A. J. Ross, G.-b. Zhao, Y. Wang et al., *The clustering of galaxies in the completed SDSS-III Baryon Oscillation Spectroscopic Survey: single-probe measurements from DR12 galaxy clustering - towards an accurate model*, *MNRAS* **471** (2017) 2370 [1607.03151].
- [96] R. Tojeiro, W. J. Percival, J. Brinkmann, J. R. Brownstein, D. J. Eisenstein, M. Manera et al., *The clustering of galaxies in the SDSS-III Baryon Oscillation Spectroscopic Survey: measuring structure growth using passive galaxies*, *MNRAS* **424** (2012) 2339 [1203.6565].
- [97] Z. Zhai, J. L. Tinker, C. Hahn, H.-J. Seo, M. R. Blanton, R. Tojeiro et al., *The Clustering of Luminous Red Galaxies at $z \sim 0.7$ from EBOSS and BOSS Data*, *ApJ* **848** (2017) 76 [1607.05383].
- [98] Y.-K. Chiang and B. Ménard, *Extragalactic Imprints in Galactic Dust Maps*, *ApJ* **870** (2019) 120 [1808.03294].
- [99] P. Craven and G. Wahba, *Smoothing noisy data with spline functions*, *Numer. Math.* **31** (1978) 377.

- [100] HI4PI Collaboration, N. Ben Bekhti, L. Flöer, R. Keller, J. Kerp, D. Lenz et al., *HI4PI: A full-sky H I survey based on EBHIS and GASS*, *A&A* **594** (2016) A116 [[1610.06175](#)].
- [101] S. Ferraro and J. C. Hill, *Bias to CMB Lensing Reconstruction from Temperature Anisotropies due to Large-Scale Galaxy Motions*, *Phys. Rev.* **D97** (2018) 023512 [[1705.06751](#)].
- [102] E. Kitanidis, M. White, Y. Feng, D. Schlegel, J. Guy, A. Dey et al., *Imaging Systematics and Clustering of DESI Main Targets*, *arXiv e-prints* (2019) arXiv:1911.05714 [[1911.05714](#)].
- [103] A. H. Wright, H. Hildebrandt, J. L. van den Busch and C. Heymans, *Photometric Redshift Calibration with Self Organising Maps*, *arXiv e-prints* (2019) arXiv:1909.09632 [[1909.09632](#)].
- [104] H. Hildebrandt, F. Köhlinger, J. L. van den Busch, B. Joachimi, C. Heymans, A. Kannawadi et al., *KiDS+VIKING-450: Cosmic shear tomography with optical and infrared data*, *A&A* **633** (2020) A69 [[1812.06076](#)].
- [105] R. G. Kron, *Photometry of a complete sample of faint galaxies.*, *ApJS* **43** (1980) 305.
- [106] O. Le Fèvre, P. Cassata, O. Cucciati, B. Garilli, O. Ilbert, V. Le Brun et al., *The VIMOS VLT Deep Survey final data release: a spectroscopic sample of 35 016 galaxies and AGN out to $z \sim 6.7$ selected with $17.5 \leq i_{AB} \leq 24.75$* , *A&A* **559** (2013) A14 [[1307.0545](#)].
- [107] C. J. Lonsdale, H. E. Smith, M. Rowan-Robinson, J. Surace, D. Shupe, C. Xu et al., *SWIRE: The SIRTf Wide-Area Infrared Extragalactic Survey*, *Publ. Astron. Soc. Pac.* **115** (2003) 897 [[astro-ph/0305375](#)].
- [108] P. Franzetti, M. Scodreggio, B. Garilli, D. Vergani, D. Maccagni, L. Guzzo et al., *The VIMOS-VLT deep survey. Color bimodality and the mix of galaxy populations up to $z \sim 2$* , *A&A* **465** (2007) 711 [[astro-ph/0607075](#)].
- [109] M. J. I. Brown, Z. Zheng, M. White, A. Dey, B. T. Jannuzi, A. J. Benson et al., *Red Galaxy Growth and the Halo Occupation Distribution*, *ApJ* **682** (2008) 937 [[0804.2293](#)].
- [110] C. Conroy, R. H. Wechsler and A. V. Kravtsov, *Modeling Luminosity-dependent Galaxy Clustering through Cosmic Time*, *ApJ* **647** (2006) 201 [[astro-ph/0512234](#)].
- [111] Z. Zheng, A. A. Berlind, D. H. Weinberg, A. J. Benson, C. M. Baugh, S. Cole et al., *Theoretical Models of the Halo Occupation Distribution: Separating Central and Satellite Galaxies*, *ApJ* **633** (2005) 791 [[astro-ph/0408564](#)].
- [112] Planck Collaboration, P. A. R. Ade, N. Aghanim, C. Armitage-Caplan, M. Arnaud, M. Ashdown et al., *Planck 2013 results. XVI. Cosmological parameters*, *A&A* **571** (2014) A16 [[1303.5076](#)].
- [113] M. White, *The Mass Function*, *ApJS* **143** (2002) 241 [[astro-ph/0207185](#)].
- [114] C. W. Stark, M. White, K.-G. Lee and J. F. Hennawi, *Protocluster discovery in tomographic Ly α forest flux maps*, *MNRAS* **453** (2015) 311 [[1412.1507](#)].
- [115] K. Heitmann, Z. Lukić, P. Fasel, S. Habib, M. S. Warren, M. White et al., *The cosmic code comparison project*, *Computational Science and Discovery* **1** (2008) 015003 [[0706.1270](#)].
- [116] J. Tinker, A. V. Kravtsov, A. Klypin, K. Abazajian, M. Warren, G. Yepes et al., *Toward a Halo Mass Function for Precision Cosmology: The Limits of Universality*, *ApJ* **688** (2008) 709 [[0803.2706](#)].
- [117] J. L. Tinker, B. E. Robertson, A. V. Kravtsov, A. Klypin, M. S. Warren, G. Yepes et al., *The Large-scale Bias of Dark Matter Halos: Numerical Calibration and Model Tests*, *ApJ* **724** (2010) 878 [[1001.3162](#)].
- [118] R. K. Sheth and G. Tormen, *Large-scale bias and the peak background split*, *MNRAS* **308** (1999) 119 [[astro-ph/9901122](#)].

- [119] R. K. Sheth, H. J. Mo and G. Tormen, *Ellipsoidal collapse and an improved model for the number and spatial distribution of dark matter haloes*, *MNRAS* **323** (2001) 1 [[astro-ph/9907024](#)].
- [120] J. Comparat, F. Prada, G. Yepes and A. Klypin, *Accurate mass and velocity functions of dark matter haloes*, *MNRAS* **469** (2017) 4157 [[1702.01628](#)].
- [121] J. Bovy, A. D. Myers, J. F. Hennawi, D. W. Hogg, R. G. McMahon, D. Schiminovich et al., *Photometric Redshifts and Quasar Probabilities from a Single, Data-driven Generative Model*, *ApJ* **749** (2012) 41 [[1105.3975](#)].
- [122] N. P. Ross, A. D. Myers, E. S. Sheldon, C. Yèche, M. A. Strauss, J. Bovy et al., *The SDSS-III Baryon Oscillation Spectroscopic Survey: Quasar Target Selection for Data Release Nine*, *ApJS* **199** (2012) 3 [[1105.0606](#)].
- [123] M. A. Strauss, D. H. Weinberg, R. H. Lupton, V. K. Narayanan, J. Annis, M. Bernardi et al., *Spectroscopic Target Selection in the Sloan Digital Sky Survey: The Main Galaxy Sample*, *AJ* **124** (2002) 1810 [[astro-ph/0206225](#)].